Development of ultra-low cycle fatigue life prediction model for structural steel considering the effects of surface roughness, loading frequency, and loading amplitude

Abstract

Abrasive blast cleaning is often done for steel structures before applying various protective coatings, which produces rough surfaces with changes in fatigue properties. This problem has been addressed in the low- and high-cycle fatigue regimes; however, the effect of surface roughness in combination with different loading parameters on the ultra-low cycle fatigue (ULCF) life has not been reported thus far. To this aim, a total of 59 ULCF tests on designed specimens of SM400 steel with five levels of surface roughness were performed under various loading frequencies and displacement amplitudes. The analysis of experimental results indicates a substantial reduction in fatigue life with an increase in the surface roughness and loading amplitude and a decrease in the loading frequency. Additionally, the strength degradation, dissipation energy, and load–displacement curves are discussed in detail. With the use of experimental data, a new life prediction model characterizing the combined effects of surface roughness, loading frequency, and loading amplitude on the ULCF life is proposed. Moreover, the proposed model is validated by predicting the fatigue life under variable and constant loading amplitude patterns. Comparison between experimental and theoretical results shows that the proposed model accurately estimates the ULCF life within an error band of $\pm$15%, with a reasonable selection of model parameters.

Keywords: loading amplitude, loading frequency, life prediction, surface roughness, structural steel, ultra-low cycle fatigue

Nomenclature:

R_z	10-point mean roughness	N_f	Experimental fatigue life
R_{zr}	Reference surface roughness	N_r	Reference fatigue life
R_a	Arithmetic mean deviation	$N_{f,p}$	Predicted fatigue life
R_q	Root mean squared height	$\Delta\varepsilon$	Strain range
R_t	Total profile height	$\Delta\varepsilon_{eq}$	Equivalent strain range
c_1, α	Model parameters related to Coffin-Manson's relationship	c_2, β	Model parameters related to equation (5)
c_3, γ	Model parameters related to equation (8)	c_4, η	Model parameters related to equation (17)
n_i	Number of cycles corresponding to the *i*th displacement range	f f_r	Loading frequency Reference loading frequency
ρ	Radius of curvature	R^2	Coefficient of determination
ε	Evaluated strain	z	Surface height
b	Distance of neutral axis from surface	d	Displacement amplitude
R	Displacement ratio		
Acronyms			
ULCF	Ultra-low cycle fatigue	LCF	Low cycle fatigue
AASHTO	American Association of State Highway and Transportation Officials	ASTM	American Society for Testing and Materials
JIS	Japanese Industrial Standard	CA	Constant loading amplitude
VA	Four-step incremental loading	VB	Varying mean loading amplitude
VC	Two-step incremental loading	PE	Percentage error
APE	Average percentage error	SD	Standard deviation
RCSC	Research Council for Structural Connections	JASS	Japanese Architectural Standard Specifications
ISO	International Organization for Standardization		

1 Introduction

Failure of structural steel members under strong cyclic excitation was observed in steel braces, welded beam-column connections, and steel bridge piers during the historical Kobe earthquake of 1995 and the Northridge earthquake of 1994 (Miller, 1998; Nakashima et al., 1998; Tamura et al., 2018). In low cycle fatigue (LCF), failure is characterized by crack initiation that propagates under cyclic reversals and ultimately emerges as a fracture (Xue, 2008). A phenomenon whereby enormous strain amplitudes are applied and fracture occurs after experiencing dozens to hundreds of cycles is termed ultra LCF (ULCF) (Lee et al., 2022; Wang et al., 2021). It has been investigated that when the number of loading cycles falls below approximately 200, the strain life relation may deviate from Coffin-Manson's relation because of the change in damage mechanisms (Kuroda, 2002; Nip et al., 2010; Xiang et al., 2017). Metal structures are prone to plastic deformation under strong cyclic excitations, such as destructive earthquakes. Damage to structures is associated with the unstable behavior of thin-walled members in steel braces owing to the large plastic deformations with the beginning of local buckling. When structures experience extreme earthquakes, a major part of the damage occurs within hundreds of loading cycles, which induces concentrated larger cyclic deformation with loading reversals and eventually leads to ductile fracture (Jia et al., 2014; Jia and Ge, 2018; Park et al., 2004). According to the American Association of State Highway and Transportation Officials (AASHTO, 2012) LRFD bridge design specifications, investigation entirely based on inelastic modeling may be required for limit states in case of extreme events. Therefore, considering the ULCF fracture as a limit state for the seismic design of steel structures is suggested.

The LCF life of structural steel has been comprehensively studied by considering the parameters of strain range, loading frequency, and temperature, and can be predicted using the Coffin–Manson relationship (L. F. Coffin, 1954). Recently, researchers have proposed modified Coffin–Manson models to improve the life prediction accuracy in the ULCF regime. Tateishi et al., (2007) established a prediction model in an extremely LCF regime by introducing the concept of damage mechanics under variable loading amplitude. Ge and Kang (2012) proposed a damage index for evaluating ductile crack initiation in steel members by combining Miner's rule (Miner, 1945) and Coffin–Manson model and validated this index for steel bridge piers. Xue (2008) established a unified expression for the prediction of LCF and ULCF life using material parameters and an exponential function. Li et al., (2020) modified the Coffin–Manson model by including the effects of stress triaxiality for the prediction of ULCF fracture in steel. Through this model, empirical relations were established between stress triaxiality and model parameters. Tamura et al., (2009) explored the effect of stress triaxiality on brittle fractures in steel bridge bents under severe earthquakes. A deformation history-based approach for damage evaluation of steel members under the ULCF regime was also adopted (Xie et al., 2020). This model could predict fatigue life from the displacement history of structures with the application of Miner's rule and life curves. Moreover, a prediction model considering the buckling effect was proposed for investigating ductile fracture in bracing members under an extremely LCF regime (Xu et al., 2020). This model was efficient for predicting the initiation and propagation of fracture by incorporating the effects of stress triaxiality and load angle. Salawdeh and Goggins (2013) incorporated a fatigue model to steel brace members for predicting their structural performance under cyclic loading. Moreover, seismic loading includes both cyclic and dynamic characteristics (Wang et al., 2021), and actual structures also respond to extreme earthquakes in a dynamic manner. However, the discussed models were based only on large strain amplitudes and ignored the parameter of loading frequency. Hence, incorporating and investigating the effect of frequency on the ULCF life of structural steel are required.

During earthquakes, steel structures in local areas endure both large strain and high frequency loading (Tamura et al., 2012) and existing studies have explored the effects of loading rate on their LCF life. Luo et al., (2013) investigated the effects of frequency from 0.001 to 3 Hz subjected to constant strain amplitude and observed an increase in fatigue life with the frequency until a transition strain rate value of 0.01 /sec after which the phenomenon reversed. Another study by Kanchanomai et al., (2003) developed a frequency modified Coffin–Manson relationship for a eutectic solder and observed that the fatigue ductility coefficient was highly influenced by the loading frequency ranging from 0.001 to 1 Hz. Reddy, et al., (2015a, 2015b) studied the effect of strain rate in combination with varying nitrogen content on the substructural changes and cyclic deformation occurring in 316LN stainless steel and found the predominance of thermal recovery over dynamic strain aging. For illustrating the order of loading rate under earthquake, existing studies asserted the possibility of strain rate increasing to approximately 1.0 /sec during an earthquake, corresponding to a loading frequency of 5 Hz at the local areas of steel bridge piers during the earthquake of 1995 (Sinsamutpadung et al., 2016; Sinsamutpadung and Sasaki, 2018), while another study by Tamura et al., (2012) also highlighted the possibility of strain rate reaching approximately 1.5 /sec in P75 steel bridge pier under cyclic loading. However, all these investigations were conducted in the LCF region. To create a realistic condition of extreme earthquakes in the ULCF regime, the parameters of strain amplitude and loading rates covering quasi-static to dynamic conditions should be considered. Therefore, all the experiments conducted for this study were configured to replicate these conditions.

Usually, metal structures including steel bridges undergo abrasive blasting treatment to rough the surface of substrates before the application of adhesive coatings to remove corrosion, dirt, grease, scratches, or any foreign material. Although the treatment assures a better coating adhesion, it reduces the service life of the structures (FHWA, 2015; Kainuma, 2021; NILIM, 2020). Researchers have observed a significant impact of surface roughness on the fatigue life of steel subjected to cyclic loading. Generally, fatigue cracks originate from the surface (Hasunuma et al., 2019); thus, the parameter of roughness cannot be neglected in real engineering practices. The extent of surface roughness causes high strain concentration, lowers the capacity to resist fatigue damage, and ultimately reduces the fatigue life of materials (Wang et al., 2017). Pegues et al., (2018) analyzed the size and effect of surface roughness on a high cycle fatigue regime by designing a number of additively manufactured Ti-6Al-4V specimens and concluded that the fatigue life was more sensitive to bar diameter than to the surface area. Wang et al., (2016) developed the Giga-fatigue life prediction model by employing energy theory to investigate the fracture development in FV520B-I steel, taking surface roughness as the primary variable. In addition to the experimental research, Singh et al., (2019) adopted a microstructure-based approach for modeling the impact of surface roughness on tensile fatigue. Average roughness was measured by optical surface profilometry and reduction in fatigue strength with an increase in surface roughness was predicted. Wang et al., (2013) studied the evolution of surface roughness in 316L stainless steel under LCF and indicated that an increase in surface roughness at early fatigue life and slip band formation were the main causes of the phenomenon. Some studies investigated the effect of blasting on fatigue life. Poorna Chander et al., (2009) grit blasted steel substrates using alumina of several sizes by varying time, angle, pressure, and stand-off distance to check their effect on surface roughness. They observed an increase in the subsurface hardness and residual stress with the considered parameters. McKelvey and Fatemi (2012) checked the fatigue life of forged steel and developed life curves as a function of hardness based on their experimental findings. Song et al., (2021a, 2021b) investigated the ULCF properties and fracture process of corroded steel and found that fatigue life is significantly reduced by the increasing level of surface roughness induced by the corrosion process. Additionally, processing parameters are known to have a strong impact on fatigue life, and variation in surface morphology largely affects the LCF life (Hasunuma et al., 2019). Thus, investigating the effect of surface roughness, produced by blasting, on the ULCF life is important. Considering the literature, the existing models evidently lack the ability to investigate the fatigue failure induced by surface roughness for structural steel. Moreover, the parameters of surface roughness in combination with loading frequency and loading amplitudes are important and should not be neglected during the model development of metals in the ULCF regime.

Thus far, no consensus has been achieved on investigating the combined effects of surface roughness, loading frequency, and loading amplitude on the ULCF life of structural steel. Thus, this study focuses on the development of a new ULCF life prediction model by conducting a total of 59 displacement controlled ULCF tests on notched steel specimens with different surface roughness. The load response, dissipated energy response, and load–displacement curves of the ULCF tests for processed specimens under different loading frequencies and loading amplitudes are analyzed through focused experimentation. A laser scanning technique was used to find the strain directly during the experiment by using the radius of curvature. Based on the experimental data, a new ULCF life prediction model with surface roughness coupling the effects of loading frequency and loading amplitude is proposed. Constant amplitude test results are utilized for calibrating the model parameters by performing regression analysis. Lastly, the proposed method is verified by the comparison of experimental and predicted fatigue life under constant and variable loading amplitude tests. The presented simplified model is a first of its kind as it combines all model parameters related to surface roughness, loading frequency, and loading amplitude and is expected to find application in improving the design guidelines for steel structures subjected to extreme loading conditions.

2 Experimental program

2.1 Material and test specimens

All considered specimens were composed of mild steel plate JIS-SM400 (JIS G 3106, 2004) equivalent to ASTM A283 (American Society for Testing and Materials), which is a broadly used steel for the construction of welded structures in Japan. Monotonic tensile tests at the quasi-static and dynamic displacement rates of 0.025 and 25 mm/sec, respectively, were performed on coupon specimens for obtaining the mechanical properties of the test material. Figure 1(a) illustrates the specimen geometry, while the chemical composition and material properties of SM400 steel are summarized in Table 1. The true stress–strain curves attained from the tension test at different displacement rates are shown in Figure 1(b).

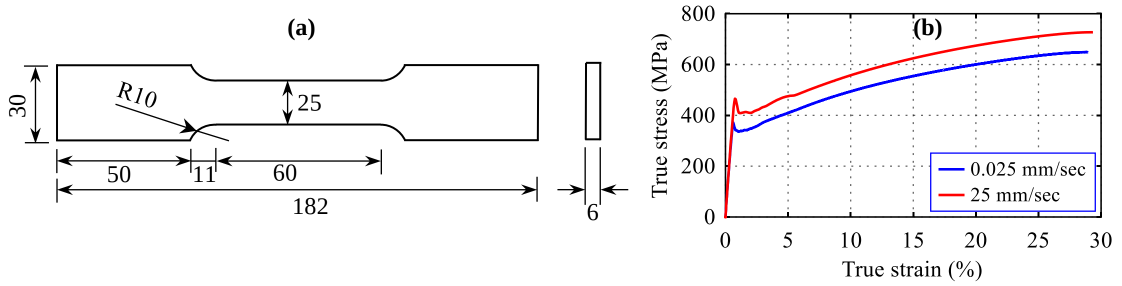

Figure 1. Tensile Test (a) Configuration of coupons for the tensile test (dimensions are in units of mm) (b) Comparative true stress–strain relationships

Table 1. Mechanical and chemical properties of SM400 steel

Test steel	Disp. rate (mm/sec)	Yield stress (MPa)	Tensile stress (MPa)	Chemical composition (%wt)				
				C	Si	Mn	P	S
SM400	0.025	372	649	0.15	0.22	0.84	0.019	0.007
	25	462	727					

For investigating the behavior of structural steel under various loading conditions, uniaxial fatigue tests were conducted on double-edge notched steel specimens, shown in Figure 2. All tension and fatigue test specimens were prepared from the same 6 mm thick SM400 steel plate. Since surface blasting was performed at the central region of 20×43.5 mm^2 (region “b”), applying a large strain amplitude at the same location for fracture occurrence was necessary. For achieving this goal, semicircular notches of radius 10 mm were formed in regions “a, b, and c”. After load application, plastic hinges were developed in regions “a and c”, while a large strain was developed in observation region “b”. A moderate notch radius was chosen to prevent the uncertainty of crack and fracture formations outside the observation region and maintain a constant buckling length. Moreover, the specimen length was kept at 280 mm for producing the buckling phenomenon. Briefly, the experimental method was established in such a way that ① a large amplitude cyclic loading was generated at the central region “b” using buckling deformation of the specimens (Tateishi et al., 2007), ② the deformation was concentrated at region “b” of the specimens through side notches and ③ strain from the central region curvature was directly evaluated in a non-contact manner by laser scanning (Saleem et al., 2022). Since the curvature of steel specimens was concentrated at their center, the location of the fracture was localized. The specimens were designed to simulate the local buckling behavior of steel members i.e., steel plates, and steel braces for clarifying failure under ULCF loading (Park et al., 2004; Tateishi et al., 2007).

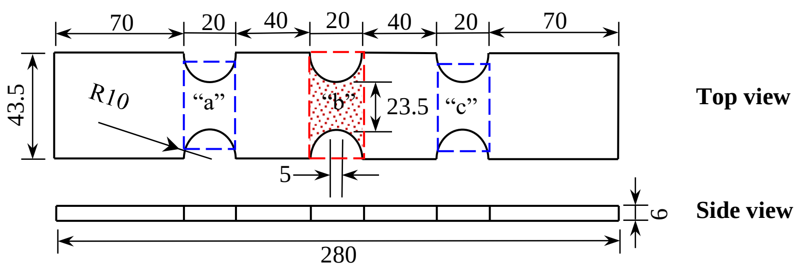

Figure 2. Geometry of specimens for fatigue tests (dimensions are in units of mm), where “b” is the region of surface treatment

2.2 Introduction and measurement of surface roughness

As per the International Organization for Standardization (ISO 8501, 2007; ISO 8503-1, 2012) guidelines, abrasive blasting is usually done on metal surfaces for the application of paint and other protective coatings. During the process, rust, mill scale, and other unwanted contaminants are removed from the surface. Thus, abrasive blasting with different surface roughness can significantly affect fatigue strength. To investigate the effect of surface roughness on ULCF life, flat surfaces of steel specimens were blasted to achieve 10-point mean roughness R_z of five different levels 20, 40, 60, 80, and 100 μm in this study. In Japanese Industrial Standard (JIS B 0601, 2013), rough profiles are represented by parameter R_z because it is more sensitive to occasional deep valleys or high peaks than arithmetic mean roughness R_a; hence, the roughness was indicated by the parameter R_z. The recommended values of the surface roughness R_z for blast-cleaned steel surfaces range from 25 to 80 μm, with a maximum value of 100 μm, according to ISO 8503-1, (2012). The Japanese Architectural Standard Specification (JASS 6, 2007) recommends carrying out the surface blasting treatment resulting in surface roughness of less than 100 μm for steel metal cut surfaces and surface roughness R_z of larger than 50 μm in case of high strength bolted connections to achieve the friction coefficient of 0.45 (Nakajima et al., 2011). Moreover, for thermally cut holes of bolted connections which are explicitly allowed in buildings, the surface roughness should not exceed 25 μm as per the Research Council on Structural Connections (RCSC, 2020) guidelines. So, the surface roughness levels of abrasive surfaces employed in this study were selected accordingly. Since the goal of this study is to evaluate the effect of fine to rough surfaces, combined with other loading parameters, on the ULCF life of structural steel, so by using different combinations of machining parameters, such as abrasive type, shape, and size; blasting pressure; and nozzle distance, five different values of R_z, ranging from 20 to 100 μm, were obtained. The adopted machining parameters and conditions for abrasive blasting are listed in Table 2.

The surface roughness of the specimens was measured with a roughness measuring device, Surftest SV-2000 (Mitutoyo, Japan) that provides a two-dimensional (2D) surface profile. Measurements were conducted using a tip radius of 2 μm, range of 800 μm, measurement pitch of 0.001 μm, and lower and upper cut-off wavelengths of 0.008 and 2.5 mm, respectively. The representative 2D roughness profiles along the longitudinal direction (y-direction in Figure 17) for five different cases are illustrated in Figure 3. These surface textures were measured over a length of 12.5 mm with repetitions at different locations. Table 3 presents the mean values of the measured R_z (10-point height), R_a (arithmetic mean deviation), R_q (root mean squared height), and R_t (total height) for a population of 10 samples for each surface condition.

Table 2. Machining parameters adopted to achieve the targeted surface roughness R_z

Machining parameters	Targeted surface roughness, R_z (μm)				
	20	40	60	80	100
Abrasive material	Alumina (A-80)	Alumina (A-36)	Alumina (A-24)	Steel grid (G-120H)	Steel grid (G-120H)
Shape of abrasive	Sharp grains	Sharp grains	Sharp grains	Sharp grains	Sharp grains
Size of abrasive	~ 0.2 mm	~ 0.5 mm	~ 0.7 mm	~ 1.2 mm	~ 1.2 mm
Blasting pressure	0.45MPa	0.50MPa	0.45MPa	0.17MPa	0.38MPa
Equipment used	SAM-6	SAM-6	SAM-6	DM-8 (AT-20)	DM-8 (AT-20)
Blasting angle	~ 90°	~ 90°	~ 90°	~ 90°	~ 90°
Blasting distance	~ 100 mm	~ 100 mm	~ 100 mm	~ 150 mm	~ 150 mm

Table 3. Mean values of evaluated roughness parameters for each surface condition

Roughness parameters (μm)	Targeted surface roughness, R_z (μm)				
	20	40	60	80	100
R_z	17.69	38.43	61.65	77.16	96.16
R_a	2.98	4.98	8.1	10.21	14.42
R_q	3.64	6.34	10.49	13.47	18.48
R_t	22.76	44.94	71.11	107.74	123.75

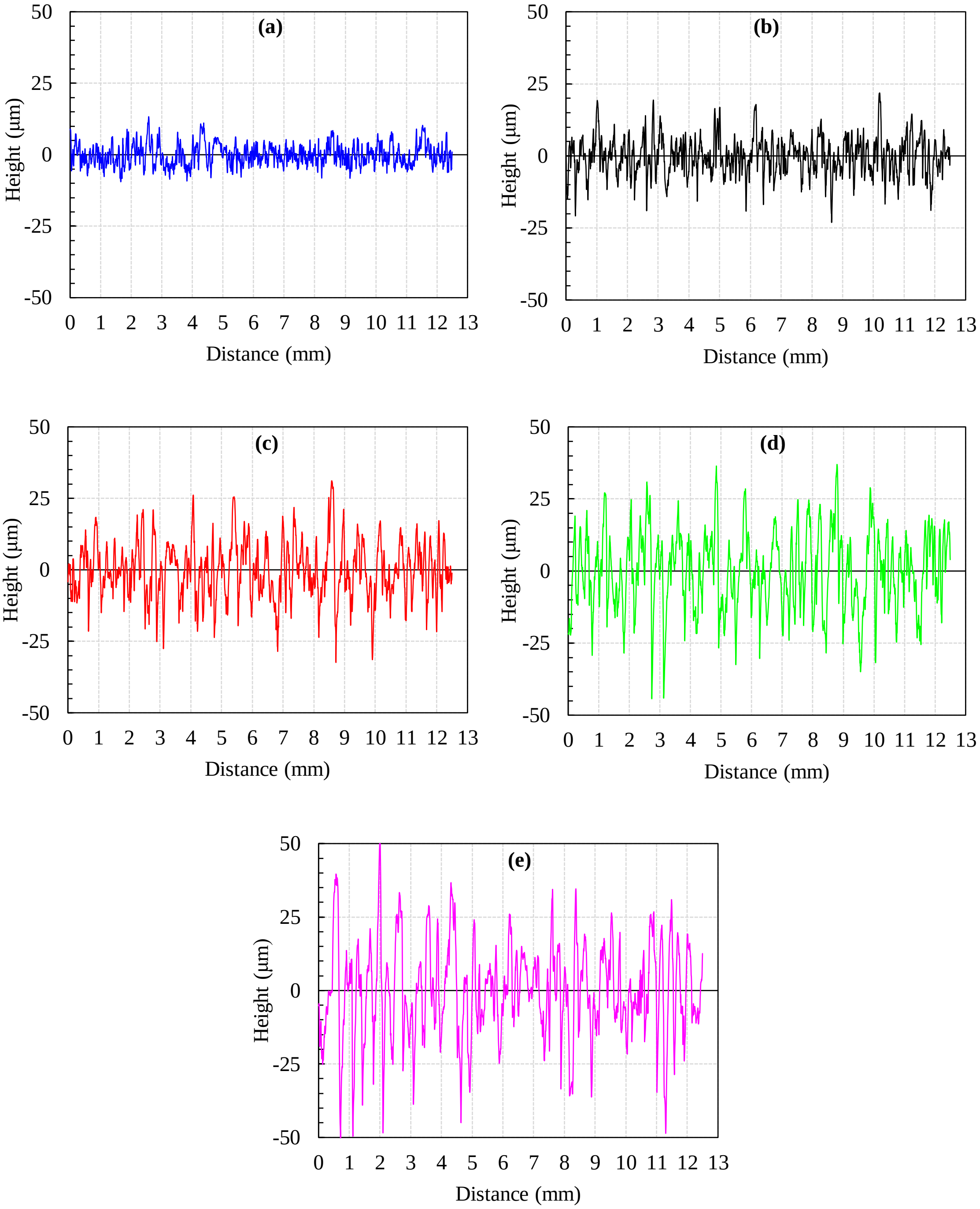

Figure 3. 2D surface roughness profiles for (a) 20, (b) 40, (c) 60, (d) 80, and (e) 100 µm

2.3 Fatigue experiment setup and procedure

A total of 59 ULCF tests were performed on notched steel specimens with variable surface roughness subjected to various loading conditions. A displacement-controlled cyclic loading protocol with a displacement ratio $R = \mathrm{dmin}/\mathrm{dmax} = 0$, having a triangular waveform, was used to ascertain the process of ULCF fracture formation. Tests were performed at room temperature employing an electrohydraulic servo testing machine (EHF-EV200kN, Shimadzu, Japan) with a loading capacity of 200 kN. The experimental testing system is shown in Figure 4. The top end of the test specimen was fixed, while the bottom end was free in the longitudinal direction. The rotational degrees of freedom along the longitudinal direction at the bottom were free, while the other two rotational degrees of freedom were fixed. The feedback to control the input displacement was obtained from the displacement transducer attached to the actuator of the machine. A default displacement transducer was built into the actuator of the machine. In this study, PID (proportional–integral–derivative) control, a fully digital and non-linear feedback control algorithm, was implemented for measuring the exact displacement and applying a high frequency loading. In addition to the algorithm, a laser scanner (KEYENCE, LJ-V7080) with a measurement pitch of 50 μm was oriented perpendicular to the center of the specimen for measuring the surface topography of the observation region, from which the strain value was directly calculated.

According to ASTM E1049-85 (2011) guidelines stating the procedure for cycle counting in fatigue analysis, N_f can be taken as the number of loading cycles that a specimen could sustain before the failure of a particular nature occurred. The loading continued until the initiation of specimen fracture, and N_f was determined corresponding to the abrupt change in the slope of load–displacement curve under tensile loading cycle (Li et al., 2021; Tian et al., 2021; Xie et al., 2020). Figure 5 shows an image of the actual specimen subjected to the fatigue test. Fracture took place across the locally buckled area at the mid-height of the specimen when it was stretched under tensile loading.

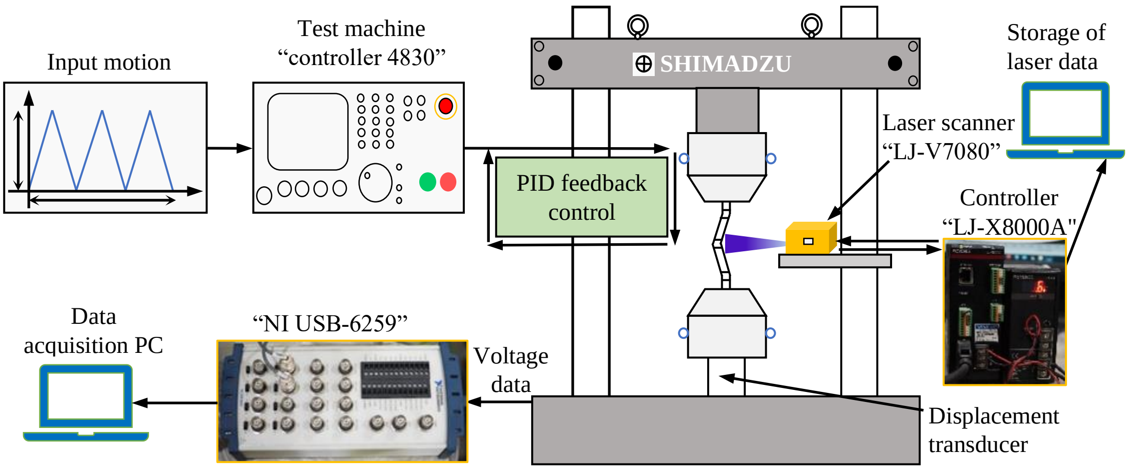

Figure 4. Schematic of experimental system and signal flow

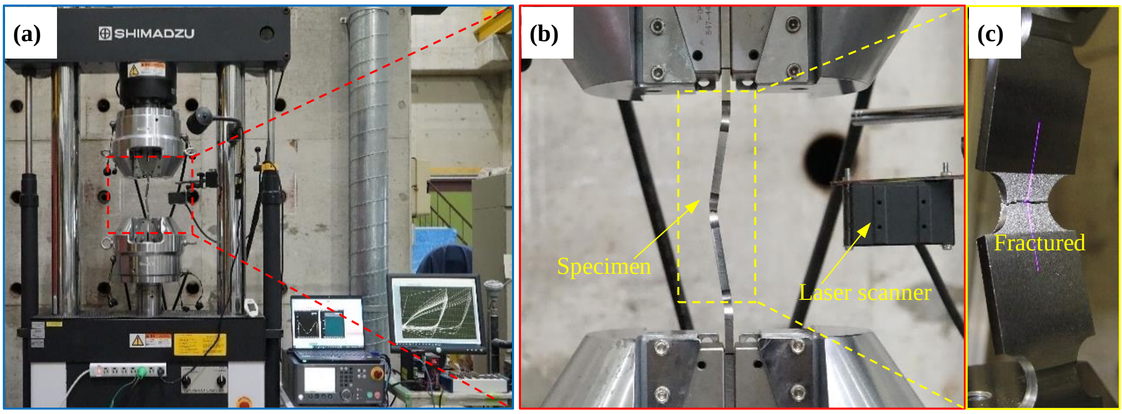

Figure 5. (a) Actual specimen setup and devices used during the experiment (b) Lateral and local buckling (c) Fracture across the locally buckled area at the mid-height of the specimen

2.4 Grouping of experimental fatigue specimens and loading conditions

To investigate the combined effects of surface roughness, loading amplitude, and loading frequency on the ULCF life of steel, 11 types of loading conditions were selected for each roughness case, and a total of 55 experiments under different surface roughness were conducted. Moreover, four additional tests were also performed on plain specimens to check the effect of blasting on fatigue life for comparison. The results are compiled and listed in Table 4. All the notations are listed in the notes at the end of Table 7. Since the characteristics of an extreme earthquake include fatigue failure under a smaller number of loading cycles of high amplitude and quasi-static to dynamic loading conditions, all experiments of this study were configured to replicate the characteristics. Test specimens were divided into three groups. The input loading conditions along with the fatigue test results are enlisted in Tables 5, 6, and 7. The test results of the first two groups (Tables 5 and 6) were used for the development/calibration of the proposed model, while the results of the third group (Table 7) were used for validating the proposed model. Since the measured R_z values of the blasted specimens were not the same as the targeted values, for convenience, the targeted roughness values were used in this study.

Table 4. Fatigue experiment results for plain specimens under constant loading amplitude

Specimen ID	R_z	d	f	$\Delta\varepsilon$	N_f
NB-CA2-0.005-Tri	No	2	0.005	0.035	153.5
NB-CA3-0.005-Tri	No	3	0.005	0.05	85.5
NB-CA4-0.005-Tri	No	4	0.005	0.065	54.5
NB-CA5-0.005-Tri	No	5	0.005	0.08	33.5

For the first group, constant loading amplitude (CA) tests were conducted on blasted specimens with five levels of surface roughness. The experimental scheme and the test results are presented in Table 5. Comparison of these results with those of plain specimens indicated that the fatigue life of blasted specimens with 100 μm roughness decreased by 1.8 times than those of plain specimens, revealing the prime effect of surface roughness on the ULCF life of metal structures. The effect was more substantial for higher values of surface roughness. This observation was explained by the presence of surface defects in blasted specimens, which was responsible for the reduction in fatigue strength. For ULCF fracture to occur, the amplitude of the input loading should exceed the yielding point and a large plastic deformation should occur at the local areas of the steel member. Therefore, a number of trial tests were done to find the amplitudes of input displacement, such that the specimen failure occurred within dozens to hundreds of loading cycles. Constant amplitude tests were conducted at displacement amplitudes of 2, 3, 4, and 5 mm under a constant loading frequency of 0.005 Hz. Since constant loading amplitude is the standard testing protocol used to characterize fatigue properties, the results of the tests were used for the calculation of material constants and calibration of the proposed model.

Table 5. Fatigue experiment results for blasted specimens under various constant loading amplitudes

Specimen ID	R_z	d	f	$\Delta\varepsilon$	N_f	$N_{f,p}$
B20-CA2-0.005-Tri	20	2	0.005	0.035	148.5	129.42
B20-CA3-0.005-Tri	20	3	0.005	0.05	77.5	69.22
B20-CA4-0.005-Tri	20	4	0.005	0.065	46.5	43.69
B20-CA5-0.005-Tri	20	5	0.005	0.08	33.5	30.35
B40-CA2-0.005-Tri	40	2	0.005	0.035	113.5	105.12
B40-CA3-0.005-Tri	40	3	0.005	0.05	66.5	56.23
B40-CA4-0.005-Tri	40	4	0.005	0.065	40.5	35.49
B40-CA5-0.005-Tri	40	5	0.005	0.08	25.5	24.65
B60-CA2-0.005-Tri	60	2	0.005	0.035	108.5	93.08
B60-CA3-0.005-Tri	60	3	0.005	0.05	59.5	49.79
B60-CA4-0.005-Tri	60	4	0.005	0.065	37.5	31.42
B60-CA5-0.005-Tri	60	5	0.005	0.08	24.5	21.83
B80-CA2-0.005-Tri	80	2	0.005	0.035	97.5	85.39
B80-CA3-0.005-Tri	80	3	0.005	0.05	50.5	45.67
B80-CA4-0.005-Tri	80	4	0.005	0.065	30.5	28.82
B80-CA5-0.005-Tri	80	5	0.005	0.08	23.5	20.02
B100-CA2-0.005-Tri	100	2	0.005	0.035	78.5	79.86
B100-CA3-0.005-Tri	100	3	0.005	0.05	48.5	42.71
B100-CA4-0.005-Tri	100	4	0.005	0.065	28.5	26.96
B100-CA5-0.005-Tri	100	5	0.005	0.08	18.5	18.73

For the second group, ULCF tests were conducted on blasted specimens under a wide range of loading frequencies from 0.005 to 5 Hz (Sinsamutpadung and Sasaki, 2018; Tamura et al., 2012), at an amplitude of 5 mm, for examining their combined effect on ULCF life. The test results are shown in Table 6. The selected frequencies covered a wide range of displacement rates, from 0.025 to 25 mm/sec, targeting the quasi-static to dynamic conditions of earthquakes. Since a majority of the available researchers conducted fatigue tests at quasi-static conditions, which hardly affected the fatigue performance (Li et al., 2020; Xie et al., 2020; Xu et al., 2020), the aforementioned frequencies were selected to simulate a real earthquake phenomenon, with a wide range of loading frequency. Moreover, while conducting experiments at high loading frequencies, testing was temporarily paused for approximately 1 min after the application of each loading cycle in order to avoid the effect of temperature rise.

Table 6. Fatigue experiment results for blasted specimens under various loading frequencies

Specimen ID	R_z	d	f	N_f	$N_{f,p}$
B20-CA5-0.005-Tri	20	5	0.005	33.5	30.35
B20-CA5-0.05-Tri	20	5	0.05	35.5	32.90
B20-CA5-0.5-Tri	20	5	0.5	38.5	35.66
B20-CA5-5-Tri	20	5	5	44.5	38.65
B40-CA5-0.005-Tri	40	5	0.005	25.5	24.65
B40-CA5-0.05-Tri	40	5	0.05	27.5	26.72
B40-CA5-0.5-Tri	40	5	0.5	29.5	28.97
B40-CA5-5-Tri	40	5	5	33.5	31.40
B60-CA5-0.005-Tri	60	5	0.005	24.5	21.83
B60-CA5-0.05-Tri	60	5	0.05	25.5	23.66
B60-CA5-0.5-Tri	60	5	0.5	28.5	25.65
B60-CA5-5-Tri	60	5	5	30.5	27.80
B80-CA5-0.005-Tri	80	5	0.005	23.5	20.02
B80-CA5-0.05-Tri	80	5	0.05	24.5	21.70
B80-CA5-0.5-Tri	80	5	0.5	25.5	23.53
B80-CA5-5-Tri	80	5	5	29.5	25.50
B100-CA5-0.005-Tri	100	5	0.005	18.5	18.73
B100-CA5-0.05-Tri	100	5	0.05	20.5	20.30
B100-CA5-0.5-Tri	100	5	0.5	20.5	22.00
B100-CA5-5-Tri	100	5	5	23.5	23.85

For the third group, blasted specimens were tested under different variable-amplitude-loading patterns for verifying the accuracy of the proposed model. Since actual structural members are also subjected to varying loading amplitude apart from constant loading amplitude, three different loading patterns that replicated seismic loading to a certain level were employed for this study as shown in Figure 6.

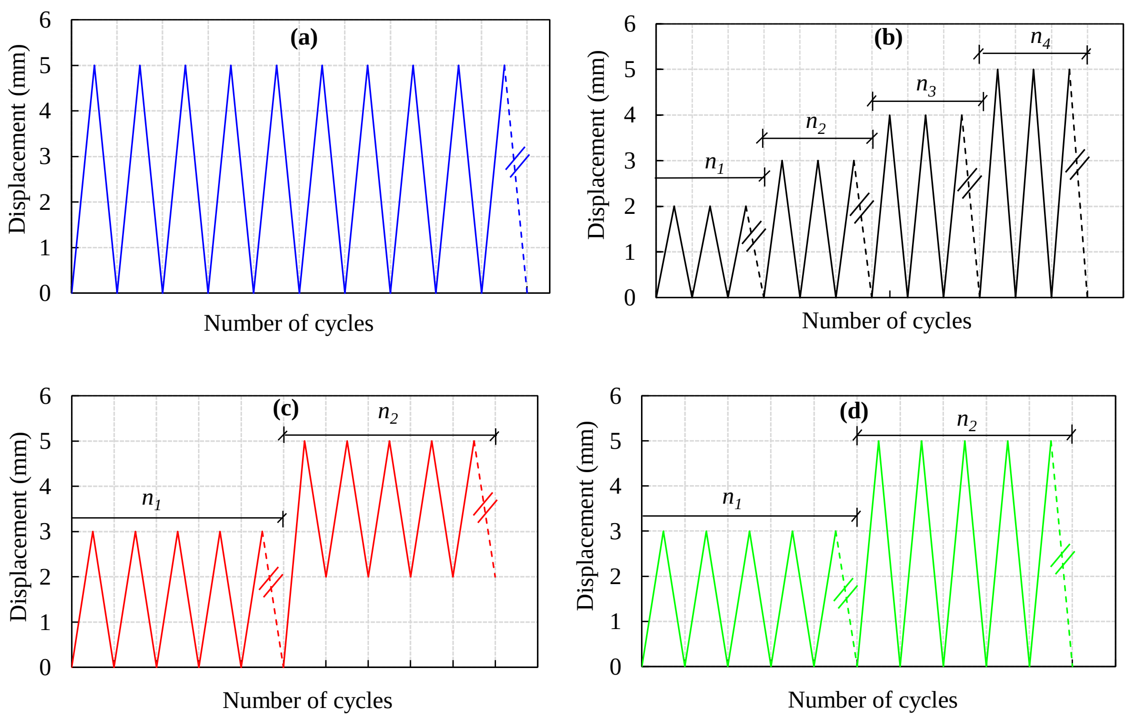

Figure 6. Loading patterns for test steel specimens. (a) CA, (b) VA, (c) VB, and (d) VC loading

The test results for this group are presented in Table 7. The loading pattern (VA) was a four-step incremental loading with imposed displacement amplitudes of 2, 3, 4, and 5 mm. This pattern was intended to simulate near field earthquakes causing large plastic deformations. The number of cycles in the first three steps with amplitudes of 2, 3, and 4 mm was calculated by taking 17% of N_f, obtained from constant amplitude tests performed at the respective amplitudes for a specific roughness case. The last step of amplitude 5 mm continued until the specimens fractured. The loading pattern (VB) was selected to study the shift in mean displacement amplitude and compare its fatigue life with the results of the 3 mm constant amplitude loading test. In this pattern, an amplitude of 3 mm was applied by shifting the mean position of the pattern. The number of cycles at the amplitude of 3 mm was calculated by taking 50% of N_f, obtained from constant amplitude tests performed at the respective displacement amplitude. After shifting the mean position, the second loading step of amplitude 3 mm continued until the specimen fractured. The loading pattern (VC) was a two-step incremental loading pattern with imposed amplitudes of 3 and 5 mm. This pattern was applied to investigate the effect of load sequence on fatigue life. The calculation for the number of cycles was the same as that for pattern VB, without any shift in mean displacement after the first loading step.

Table 7. Fatigue experiment results for blasted specimens under variable loading amplitudes

Specimen ID	R_z	Patterns	n_i	f	$\Delta\varepsilon_{eq}$	N_f	$N_{f,p}$
B20-VA-0.005-Tri	20	VA	25, 13, 8, 7.5	0.005	0.0516	53.5	65.50
B20-VB-0.005-Tri	20	VB	39, 24.5	0.005	0.05	63.5	69.22
B20-VC-0.005-Tri	20	VC	39, 10.5	0.005	0.0574	49.5	54.34
B40-VA-0.005-Tri	40	VA	19, 11, 7, 5.5	0.005	0.0517	42.5	53.02
B40-VB-0.005-Tri	40	VB	33, 17.5	0.005	0.05	50.5	56.23
B40-VC-0.005-Tri	40	VC	33, 8.5	0.005	0.0572	41.5	44.41
B60-VA-0.005-Tri	60	VA	19, 10, 6, 4.5	0.005	0.0504	39.5	49.10
B60-VB-0.005-Tri	60	VB	30, 12.5	0.005	0.05	42.5	49.79
B60-VC-0.005-Tri	60	VC	30, 8.5	0.005	0.0577	38.5	38.72
B80-VA-0.005-Tri	80	VA	18, 9, 5, 4.5	0.005	0.0503	36.5	45.19
B80-VB-0.005-Tri	80	VB	25, 13.5	0.005	0.05	38.5	45.67
B80-VC-0.005-Tri	80	VC	25, 8.5	0.005	0.0587	33.5	34.47
B100-VA-0.005-Tri	100	VA	16, 8, 5, 4.5	0.005	0.0511	33.5	41.11
B100-VB-0.005-Tri	100	VB	24, 10.5	0.005	0.05	34.5	42.71
B100-VC-0.005-Tri	100	VC	24, 7.5	0.005	0.0582	31.5	32.72

Notes: NB, Not blasted; B, blasted; CA, constant loading amplitude; VA, VB, and VC, variable loading amplitude patterns; R_z, surface roughness (μm); d, displacement amplitude (mm); n_i, number of cycles at the i^{th} displacement amplitude; f, loading frequency (Hz); $\Delta\varepsilon$, average strain range; $\Delta\varepsilon_{eq}$, equivalent strain range; N_f, experimental number of cycles to fatigue fracture; $N_{f,p}$, predicted fatigue life (cycles)

3 Experimental results and discussions

3.1 Effect of constant loading amplitude under variable surface roughness on fatigue life

This section discusses fatigue life sensitivity to constant loading amplitude of steel with different surface roughness. A total of 20 ULCF tests for five different roughness were conducted at displacement amplitudes of 2, 3, 4, and 5 mm and a loading frequency of 0.005 Hz, until the fracture of the test specimens. The specifications are listed in Table 5. The comparison result of fatigue life as a function of displacement amplitude and surface roughness is shown in Figure 7, where the numerical values at the amplitude of 2 mm represent the fatigue life N_f, while at the other displacement amplitudes, the percentage change in fatigue life is shown. For all roughness levels, a decreasing fatigue life trend was observed when displacement amplitude increased. At 2 mm, the fatigue life decreased by a factor of 1.89 equivalent to 47%, from 148.5 to 78.5 cycles, when roughness was increased from 20 to 100 μm. At a higher displacement amplitude of 5 mm, the fatigue life decreased by about 45% from 33.5 to 18.5 cycles with an increase in surface roughness from 20 to 100 μm. Song et al., (2021a) observed a similar reduction effect in the ULCF life of steel bridge piers with the increase in corrosion level. In another study by Song et al., (2021b), it was investigated that corrosion induced surface roughness has a dominant impact on the ULCF life of steel specimens. By increasing the corrosion time from 2 to 10 weeks, the average surface roughness increased by a maximum value of 6.52 μm. Test results indicated that surface roughness increased with the increase in corrosion level and the ULF fatigue life was decreased by more than 50%. Singh et al., (2019) presented a novel approach for simulating the effect of three different levels of surface roughness on the fatigue life of tensile specimens. It is depicted that an increase in the level of surface roughness reduced the fatigue lives of test specimens. Moreover, at the highest roughness level, the SN curve became steeper demonstrating that the impact of roughness is more significant at the higher fatigue cycles. McKelvey and Fatemi, (2012) investigated the fatigue life of generally employed forged steel at various hardness levels (19HRC, 25 HRC, 35HRC) by conducting rotating bending and reversed cantilever fatigue tests. These studies also pointed out that the surface finish factor is inversely proportional to the number of reversals to fatigue failure. This reduction in fatigue life can be explained by the theory of fracture mechanics, the increment in the level of surface roughness outcomes in deeper groove marks and smaller radius of bottom grains resulting in higher strain concentration, and this process ultimately decreases the resisting capacity of the material to fatigue fracture (Wang et al., 2016). Moreover, a 77% reduction in fatigue life was observed by increasing the displacement amplitude from 2 to 5 mm for a roughness value of 20 μm as in Figure 7. Thus, fatigue life was largely dependent on both loading amplitude and surface roughness, and the fatigue life obtained for a smaller roughness was the longest.

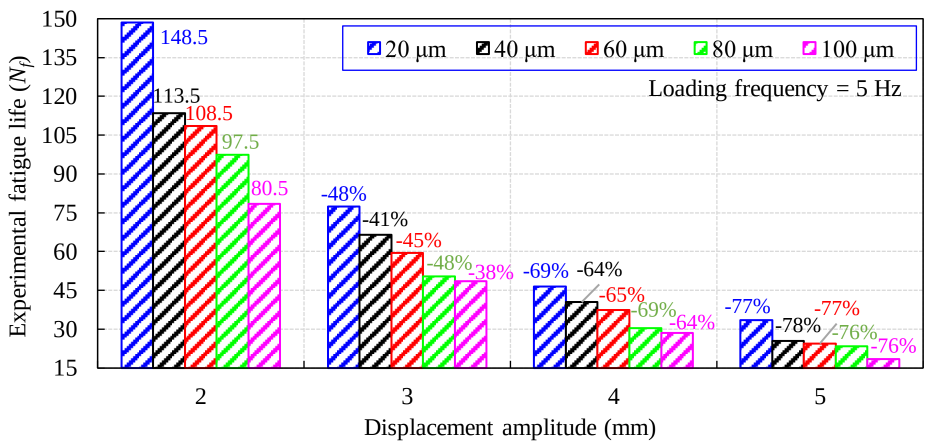

Figure 7. Comparison of fatigue life under constant loading amplitudes for different surface roughness

During the experiments, all specimens experienced local buckling at the mid-height of the specimens after surpassing the stage of yield displacement. The occurrence of local buckling caused specimens to deform by compression, while visible cracks were observed when the specimens were loaded in tension. Due to the application of successive in-elastic loading cycles, the stiffness of the buckled region deteriorated, leading to the occurrence of fracture (Salawdeh and Goggins, 2013). A comparative result of the axial load–displacement hysteresis loops for the cyclic tests are presented in Figure 8. The result elucidates that for all loading conditions, hysteresis response was not identical during the loading and unloading process due to the impact of geometrical non-linearity and in-elastic buckling. Moreover, cracks were always formed at the compression side of the central notch in the specimen during stretching, irrespective of different levels of roughness and loading conditions. This may have resulted from the high strain generated at the inner face of the specimen because of the bending deformation of test specimens. To compare the effect of different surface roughness (20, 40, 60, 80, and 100 µm) on the ULCF life, load–displacement curves have been plotted in Figure 8(a) for the case of loading amplitude of 4 mm and loading frequency of 0.005 Hz. As the fatigue life of 100 µm specimen fatigued at 4 mm amplitude and 0.005 Hz frequency is 28.5 cycles, so only the 1st and 28th cycles are presented in this figure for the purpose of comparison. These responses showed that under the similar loading amplitude, the curve area was almost similar at the 1st cycle. However, at the 28th cycle, the curve area was observed to decrease significantly by 2.81 times as the roughness varied from 20 to 100 µm. Moreover, since the fatigue experiments were conducted on specimens with variable surface roughness; however, for the sake of brevity, the hysteresis responses for the 20 µm under different loading conditions are shown in Figure 8(b to f). The load–displacement curves representing the effect of a wide range of amplitudes (2, 3, 4, and 5 mm) on the fatigue life of blasted specimens tested at 0.005 Hz are shown in Figure 8(b). For clarity, only the 1st and 33rd cycles results are shown in the figure. The area of the curve was observed to have increased by 2.85 times, as amplitude varied from 2 to 5 mm in the 1st cycle. However, the cyclic load degradation was more pronounced at higher amplitudes with the progressive increase in loading cycles. Finally, in the 33rd cycle, the area of the hysteresis loop drastically decreased at 5 mm due to the degradation in maximum load carrying capacity as a result of the fracture.

For representing the impact of constant loading amplitude on the ULCF life, dissipation energy, and load degradation analyses were conducted. Figure 9 illustrates the evolution curves of dissipation energy per cycle obtained during the complete fatigue tests, for the 20 and 100 µm cases, under various constant displacement amplitudes. Energy dissipation was evaluated by integrating the area enclosed by the load–displacement curves and is a crucial parameter for measuring the structural performance under seismic

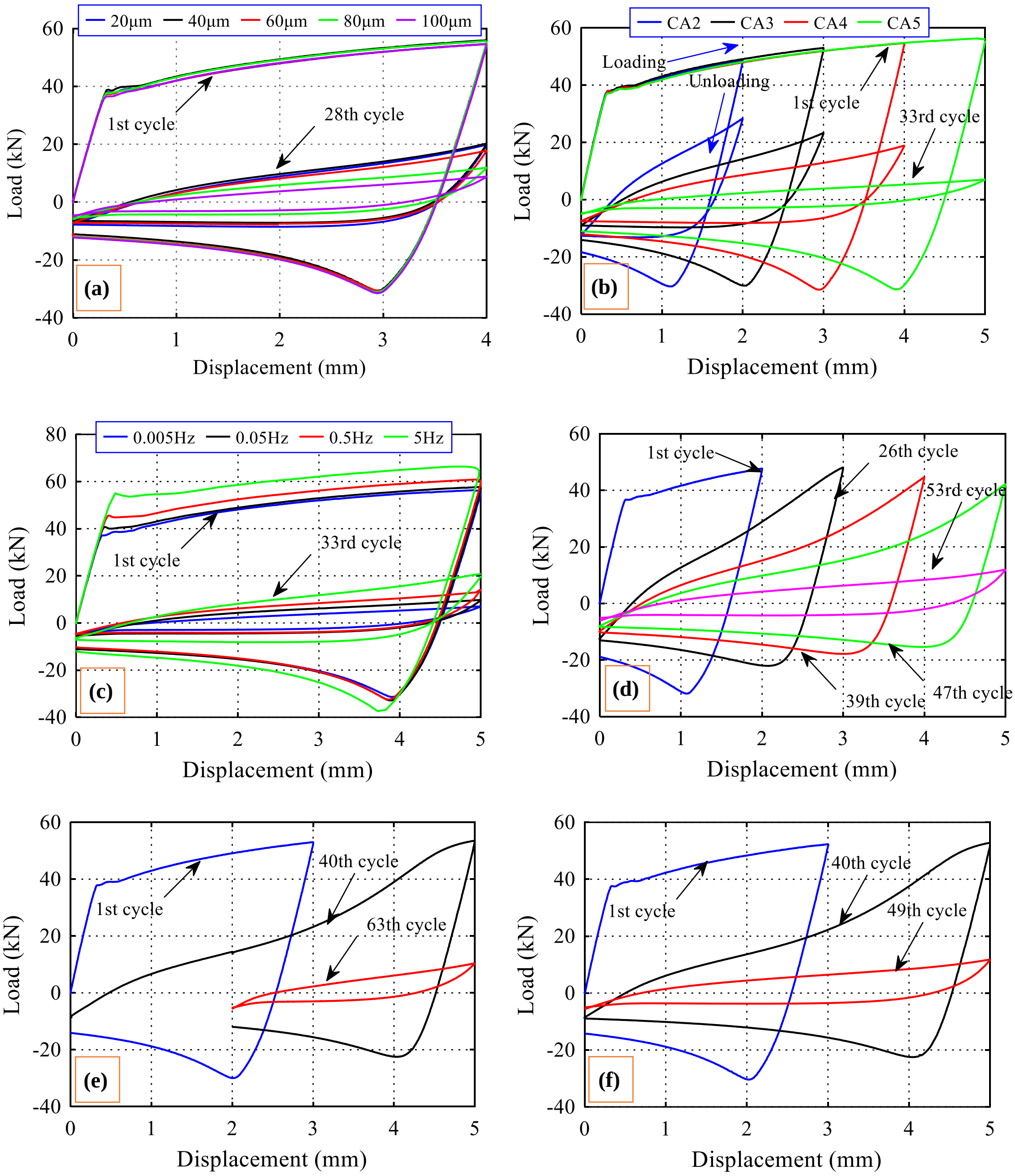

Figure 8. Hysteresis responses for (a) Specimens with variable surface roughness (b) 20 μm specimens under various loading amplitudes, (c) 20 μm specimens under various frequencies, (d) 20 μm specimens under pattern VA, (e) 20 μm specimens under pattern VB, and (f) 20 μm specimens under pattern VC

loading. From Figure 9, the tendency of energy dissipation was interpreted to be different under various loading conditions. At higher amplitudes, peak energy dissipation was observed initially which then dropped due to damage accumulation, causing a reduced fatigue life. At the beginning of the fatigue test, within the initial loading cycles, energy dissipation decreased remarkably, then stabilized, and finally dropped quickly near the state of fracture. Moreover, considering 100 µm rough specimens subjected to 5 mm loading amplitude, the cumulative energy dissipation (calculated by adding the dissipation energy of each cycle) was 1.59 times lower than that for 20 µm, showing a reduction in fatigue life. These results indicated that the surface roughness directly affected the energy dissipation capacity of the test specimens.

The cyclic load response curves for blasted specimens subjected to constant loading amplitude are shown in Figure 10. The load values above and below the zero axis represent the peak positive and negative loads during loading and unloading stages, respectively. The results implied that load degradation patterns during the process of cyclic loading and unloading were almost identical but opposite in directions. However, a remarkable difference in the absolute values of peak positive and negative loads existed. On increasing the amplitude from 2 to 5 mm, the peak positive loads increased by 1.16 and 1.18 times for 20 and 100 µm, respectively. Moreover, an expedited rate of load degradation specifically for 5 mm loading amplitude existed, resulting in lower load range; thus, indicating a decrease in fatigue life at a higher loading amplitude.

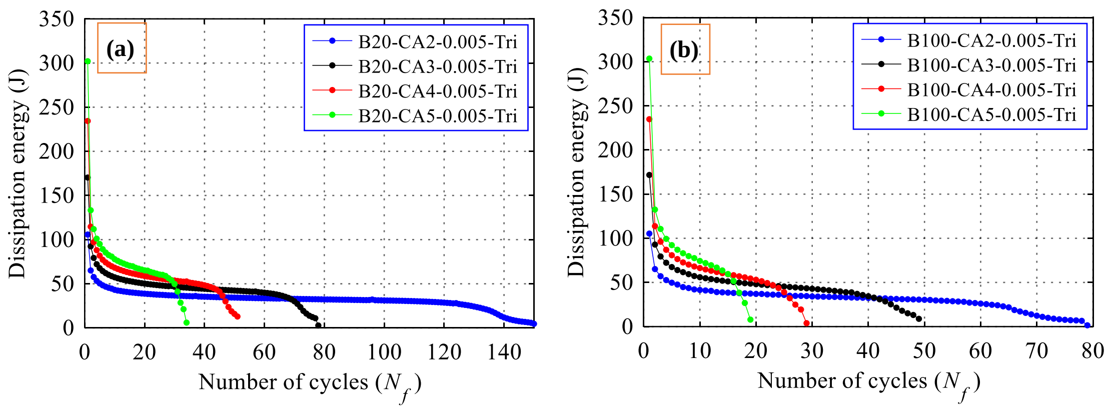

Figure 9. Influence of various constant loading amplitudes on dissipation energy for (a) 20 µm (b) 100 µm

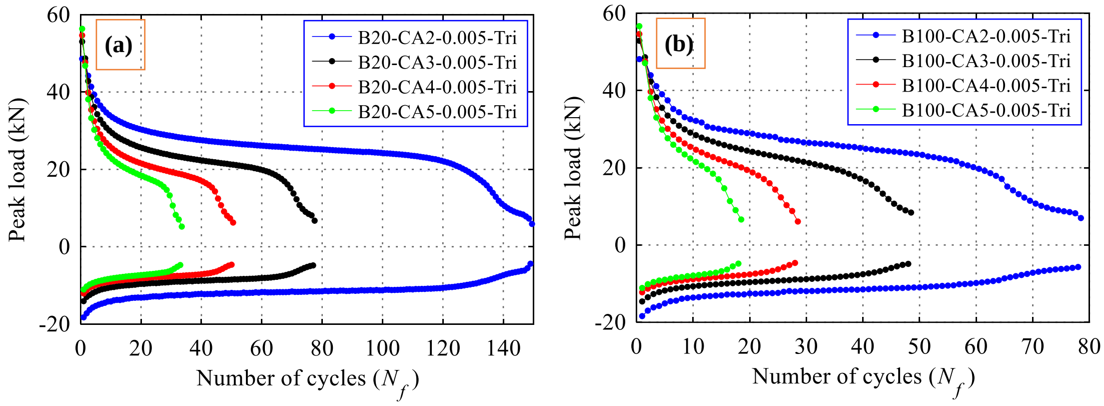

Figure 10. Influence of various constant loading amplitudes on load degradation for (a) 20 µm (b) 100 µm

3.2 Effect of loading frequency under variable surface roughness on fatigue life

This section discusses fatigue life sensitivity to the loading frequency of steel with different surface roughness. As presented in Table 6, a total of 20 ULCF tests were conducted on blasted specimens at a constant displacement amplitude of 5 mm and loading frequencies ranging from 0.005 to 5 Hz. To study the effect of loading frequency, combined with surface roughness, on fatigue life, a comparison among fatigue life obtained at different loading conditions was performed. The comparison of test results is shown in Figure 11, where the numerical values at 0.005 Hz represent the fatigue life N_f, while at other loading frequencies, the percentage change in fatigue life from 0.005 Hz is presented. A decrease in surface roughness and an increase in loading frequency led to a significant increase in fatigue life. At 0.005 Hz, the fatigue life increased by a factor of 1.81, from 18.5 to 33.5 cycles, with a decrease in surface roughness from 100 to 20 µm. At higher loading frequencies of 0.05, 0.5, and 5 Hz, a decrease in surface roughness had a similar effect. The results implied that at constant surface roughness, ULCF fatigue life was strongly dependent on the loading frequency. Moreover, an increase in loading frequency from 0.005 to 5 Hz resulted in a total of 33% increase in fatigue life, for surface roughness of 20 µm. However, the effect was less pronounced at higher values of surface roughness.

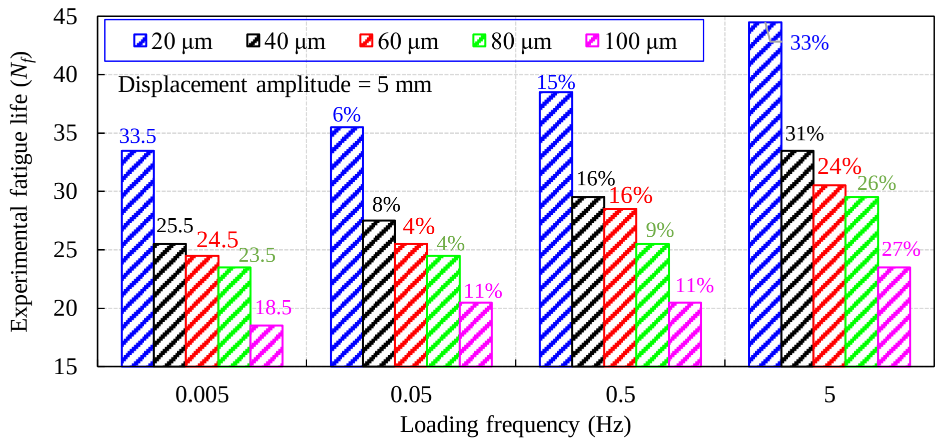

Figure 11. Comparison of fatigue life under various loading frequencies for different surface roughness

This behavior of increment in fatigue life was in agreement with the previous research work (Kanchanomai et al., 2003; Reddy et al., 2015a; Luo et al., 2013). In particular, Kanchanomai et al., (2003) conducted LCF tests on Sn-Ag eutectic solder at different frequencies ranging from 0.001 to 1 Hz and found that the fatigue ductility coefficient increases significantly with increasing frequency. The lower fatigue strength at the lower loading rate was attributed to the process of accumulated creep damage under cyclic loading. A longer loading time is needed for the experiment conducted at a smaller loading rate resulting in damage accumulation and increment in creep damage. Reddy et al., (2015a) investigated the effect of strain rate on the LCF life at higher temperatures of 773 and 873 K. The fatigue was observed to increase by around 2.5 times by increasing the strain rate from $3\text{x}10^{-5}$ to $3\text{x}10^{-3}$/sec at 773 K. The lower fatigue life at the lower loading rate was attributed to the formation of larger stress concentration at the crack tips accounting for the increased growth of cracks and reduction in fatigue strength. Moreover, the dominant mechanism controlling the deformation and fatigue strength at the higher temperature was identified to be dynamic strain gaining. On the other hand, Luo et al., (2013) conducted LCF experiments on high strength structural steel in the frequency range of 0.001 to 3 Hz under the total strain range of 2% and concluded that fatigue life majorly depends on the loading rate. An increase of about 52% in fatigue life was observed by increasing the loading frequency from 0.001 to 3 Hz. Overall, this increment in fatigue life can be explained by the fact that with the increase in loading frequency, strain hardening occurs, the temperature rises, and the material gets less time to recover itself to the original state, which causes an increment in the fatigue life of the test specimens (Luo et al., 2013).

Figure 8(c) shows the load–displacement response curves for specimens of roughness 20 μm, tested under various loading frequencies (0.005, 0.05, 0.5, and 5 Hz) and a constant amplitude of 5 mm. The results for the 1st and 33rd cycles depicted that the specimens subjected to higher loading frequencies had a steeper slope of the load–displacement curve as a result of frequency–dependent effect. Subsequently, a large area of the load–displacement curve represented a larger dissipation energy per cycle. These responses showed that under the same loading amplitude, the area of the curve increased by 1.19 times with an increase in the loading frequency, from 0.005 to 5 Hz during the 1st cycle. An increase in peak positive load with the frequency was also observed; however, this increase in the peak load was not significant from 0.005 to 0.05 Hz. In the 33rd cycle, the area of the hysteresis loop decreased drastically at 0.005 Hz, indicating the failure of the specimen. Furthermore, the influence of loading frequencies on the ULCF life was evaluated by analyzing the energy dissipation and load degradation per cycle curves.

Figure 12 illustrates the dissipation energy per cycle curves obtained after the complete process of repeated loading-unloading tests for specimens of roughness 20 and 100 μm under various loading frequencies. Higher loading frequency had a significant impact on the dissipation energy. Within the initial loading cycles, the energy dissipated per cycle decreased quickly due to buckling and then stabilized after tens of loading cycles. Eventually, the dissipation energy suddenly dropped closer to the stage of failure, accompanied by the fracture of the specimens. Moreover, considering the rough specimens tested at the frequency of 5 Hz, the cumulative energy dissipated for 100 μm was 1.68 times lesser than that for 20 μm, highlighting a reduction in fatigue life.

Graphs of cyclic load degradation under variable frequencies for both cases of surface roughness are shown in Figure 13. The results highlight that load degradation during the loading and unloading stages was not identical and specimens under higher loading frequencies tended to have a late load drop, resulting in higher load range. This delay in load drop was an indication of higher fatigue life at a higher frequency. Variation in frequency from 0.005 to 5 Hz, increased the peak positive loads by 1.17 and 1.2 times, for 20 and 100 µm, respectively. Additionally, the fatigue life sensitivity to the variation in loading frequencies was mainly reflected by the peak positive loads and not by peak negative loads. Generally, with an increase in frequency, a decrease in the final peak positive load is apparently, but the final peak negative load changes slightly.

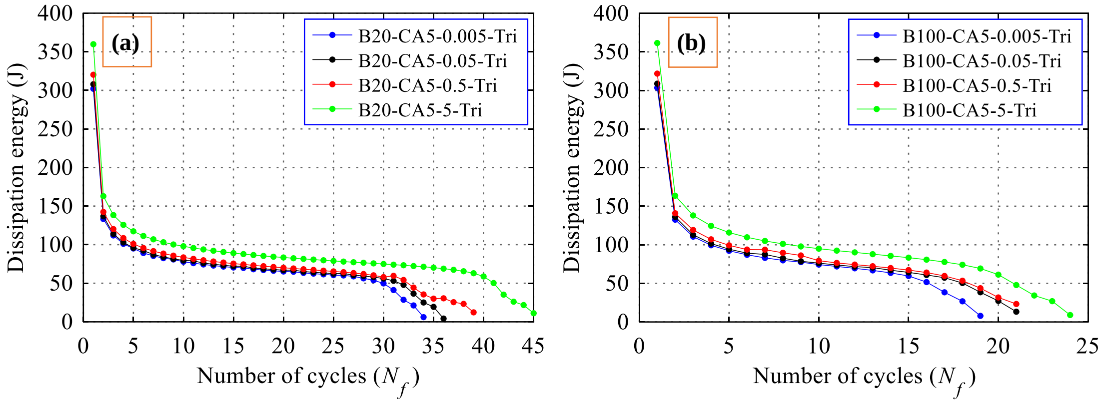

Figure 12. Influence of various loading frequencies on dissipation energy for (a) 20 µm and (b) 100 µm

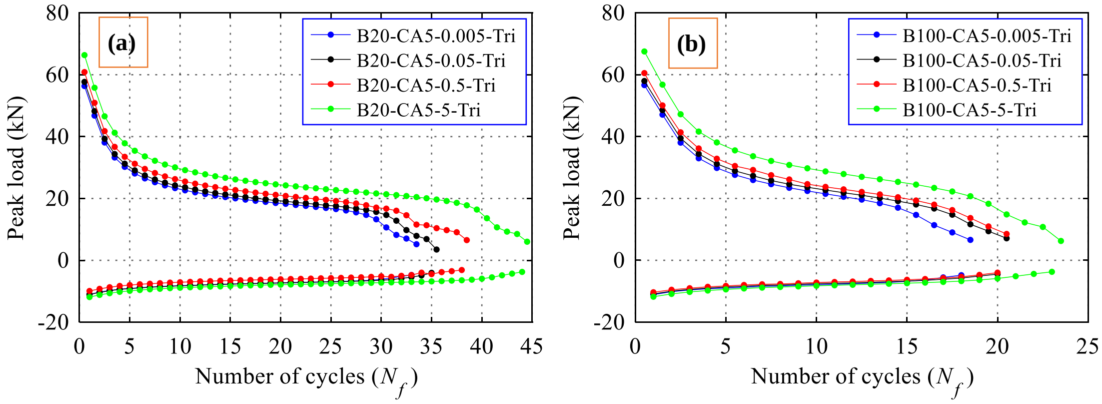

Figure 13. Influence of various loading frequencies on load degradation for (a) 20 µm and (b) 100 µm

3.3 Effect of variable loading amplitude under variable surface roughness on fatigue life

For investigating the effects of variable loading amplitude patterns on fatigue life at different levels of surface roughness, 15 ULCF tests were conducted at a frequency of 0.005 Hz. Figure 14 elucidates the dependency of fatigue life on the variable loading patterns for the blasted specimens. Under all levels of surface roughness, the specimens subjected to loading pattern "VB" had the longest fatigue life relative to the other two patterns. Therefore, the structures subjected to a loading pattern "VB" with varying mean loading amplitude were less damaged when compared to four and two-step incremental loading patterns "VA" and "VC", respectively. For 20 μm, the fatigue life under pattern "VB" was 1.18 and 1.28 times higher than that under patterns "VA" and "VC", respectively. Moreover, the number of cycles of fatigue life N_f of specimens subjected to the patterns "VB" and "VC" was lower than that of those tested at a constant amplitude of 3 mm and higher than those tested at 5 mm.

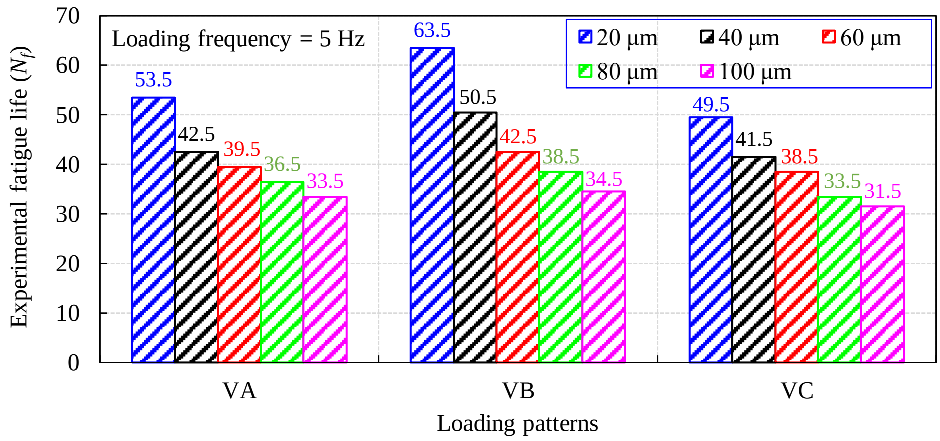

Figure 14. Comparison of fatigue life under variable loading patterns for different surface roughness

Figure 8(d, e, and f) shows the cyclic load–displacement curves of specimens having a surface roughness of 20 μm subjected to three different loading patterns at a loading frequency of 0.005 Hz. Since all the loading patterns were different, separate curves were plotted to represent the hysteresis loops after the application of each incremental loading step. For loading pattern "VA", the area surrounded by the cyclic curve was observed to have increased after the 2nd loading step, which then decreased after the 3rd and 4th loading steps. For loading patterns "VB" and "VC", an increase in the slope and area of the cyclic curve was observed after the 2nd loading step was applied. The results indicated that the effect of loading pattern "VC" on the cyclic softening behavior of the steel structures was more significant than that of the other two patterns, causing a reduction in fatigue life.

The evolution energy dissipation curves with the number of cycles under different loading patterns, for specimens of surface roughness 20 and 100 μm are shown in Figure 15. The dissipation of energy stabilized after the first few cycles, and then its value changed abruptly when the incremental loading steps were applied. However, at the last loading step, the dissipation energy was reduced abruptly due to the process of fatigue damage. Considering the specimens subjected to the "VB" pattern, the cumulative energy dissipation for 100 μm was 1.66 times lesser than that for 20 μm. In summary, major importance should be given to energy dissipation capacity for ULCF fatigue occurring under variable loading amplitude.

The cyclic load degradation curves for 20 and 100 μm rough specimens subjected to variable loading patterns are shown in Figure 16. Load degradation during the process of loading and unloading was not identical and specimens undergoing pattern "VC" tended to have an earlier load drop when compared to the other two patterns. For pattern "VA", the peak positive load value increased after the application of the 2nd step of incremental loading and then reduced with the application of the 3rd and 4th steps. However, for the loading patterns "VB" and "VC," the peak positive load increased after the application of the 2nd loading step. The strength reduction was not caused by the displacement applied beyond the ultimate stage but by the cumulative damage produced under variable loading patterns because of the fatigue phenomenon.

3.4 Calculation of strain histories

During the experiment of this study, direct measurement of the strain at the center of the specimen was challenging because the strain gauges could not be affixed to the observation surface due to buckling, and the probability of the blasted surfaces getting damaged was high. Since the curvature was localized at the

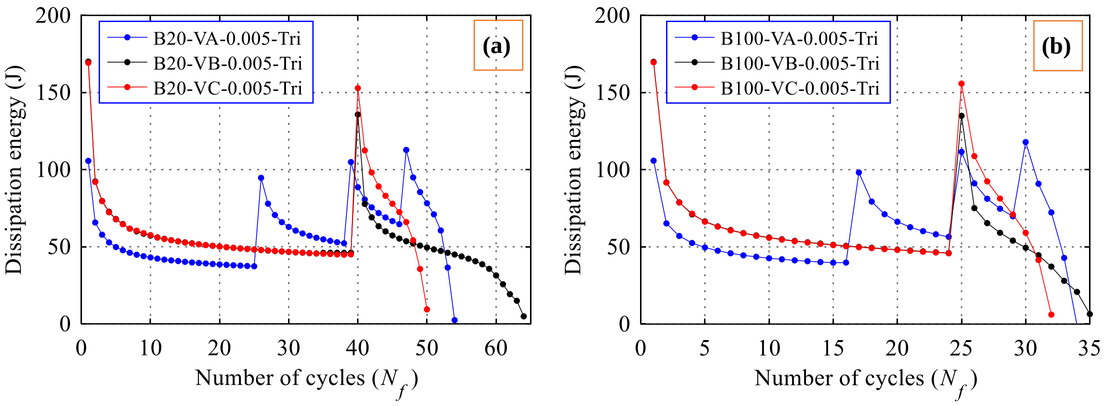

Figure 15. Influence of variable loading patterns on the dissipation energy for (a) 20 µm and (b) 100 µm

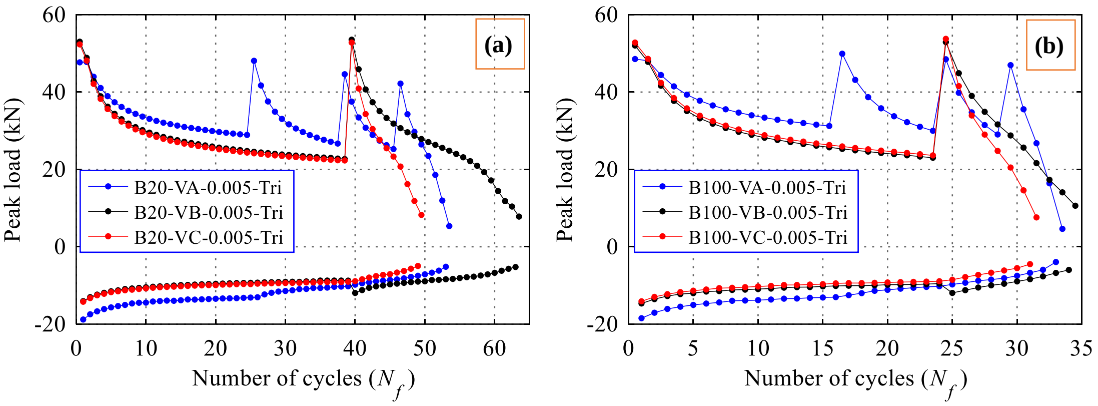

Figure 16. Influence of variable loading patterns on load degradation for (a) 20 µm and (b) 100 µm

at the center of the specimens, a method of strain evaluation, from the curvature of the specimens, using the surface height data obtained by laser displacement meter was proposed. Laser scanning was done at the compression side of the central notch after every half cycle and then the strain values were evaluated. The scanning range is highlighted by a yellow line in Figure 17. Captured surface height points were fitted by a polynomial curve (for this study, a sixth-order polynomial was employed). Then, the radius of curvature at the bottom of the curve was calculated as described in (Zhao et al., 2021). There was a difference in the radius of curvature at the compression and tension sides of test specimens. However, the current research work is focused on the fatigue life evaluation of buckling prone steel members undergoing higher bending deformation resulting in the generation of maximum strain on the compression side having a smaller radius of curvature (Park et al., 2004). Therefore, surface height data was measured only at the compression side of the middle notch to evaluate the maximum surface strain. Moreover, the change in thickness was not significant, and it was ignored to just consider the effects of surface roughness and loading frequency. Finally, after obtaining the radius of curvature, strain values were evaluated using the expressions

$$\rho = \frac{(1 + (z')^2)^{3/2}}{|z''|} \tag{1}$$

$$\varepsilon = -\frac{b}{\rho} \tag{2}$$

where ρ represents the radius of curvature in mm, z is the surface height (mm), ε is the evaluated strain value, and b denotes the distance (mm) from the neutral axis to the surface of the specimen. However, in the aforementioned expressions, the effects of Poisson's ratio were ignored. The surface curvature and its polynomial fitting curve at 1st loading cycle for B20-CA5-0.005-Tri are shown in Figure 17. The corresponding sixth-order polynomial expression is given in equation (3) and the respective R^2 value is mentioned in Figure 17.

$$z(y) = 3.06 \times 10^{-8} y^6 - 2.44 \times 10^{-7} y^5 - 3.2 \times 10^{-5} y^4 + 1.01 \times 10^{-4} y^3 + 0.018 y^2 - 0.017 y + 0.0278 \tag{3}$$

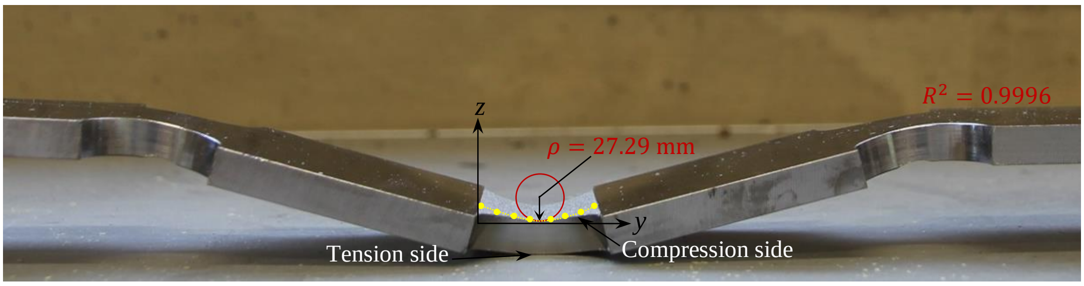

Figure 17. Determination of radius of curvature at the center of "B20-CA5-0.005-Tri" from a fitting curve at 1st cycle

Figure 18(a) illustrates the strain history obtained from the aforementioned method for “B20-CA5-0.005-Tri”. For out of plane deformation, the strain distribution was non-linear throughout the thickness of the specimen. Here ‘out of plane’ term refers to the application of load in the longitudinal direction (y-axis) of the test specimens and the resultant buckling deformation is occurring in the direction of the z-axis of the specimens. However, the initiation of failure at the surface was probable and developed inwards (Nip et al., 2010). Moreover, since the surface layer is the most important part during buckling deformation and surface treatment was also done on it, the surface strain histories were evaluated in this study. These histories were constructed by calculating the strain values after every half loading cycle. The horizontal and vertical axes represent the number of half cycles and measured values of strain. Initial axial strain after the first half cycle was evaluated by the numerical simulation method as adopted by Saleem et al., 2022. Then, this axial strain was considered in each subsequent strain value. However, this strain would not affect the magnitude of the average strain range $\Delta\varepsilon$ employed for the model development as the proposed model is based on $\Delta\varepsilon$ values which were evaluated by averaging the differences of strain values corresponding to each consecutive half and full loading cycle. Also, there would not be any effect on the proposed model parameters. The results revealed that strain at the center of the specimen increased with the progressive increase in loading cycles, which may be due to the accumulation of residual plastic deformation along with the progressive development and propagation of cracks.

Furthermore, the accuracy of the adopted strain evaluation method from the laser scanning technique was verified by conducting a numerical simulation (Saleem et al., 2022). In this study, the variation in surface topography of structural steel with variable surface treatments under fatigue loading was examined, and the experimentally obtained strain values from the surface curvature method were compared with the numerical values. Moreover, the main goal of this research is to develop a life prediction model based on large bending deformation of the test specimens, and this approach is expected to be favorable for the evaluation of larger bending deformation and large strains (Tateishi et al., 2007). Since the basic Coffin–Manson strain-based model was modified in this study to account for the combined effects of surface roughness, loading frequency, and loading amplitude, strain ranges were employed for the development of SN curves. In practical applications, strain ranges are calculated from the strain history; thus, evaluations were done using the maximum value method described by (Ge and Kang, 2012). Based on strain histories, loading amplitudes equal to 2, 3, 4, and 5 mm corresponded to approximately 3.5%, 5%, 6.5%, and 8% average strain ranges, respectively, as shown in Figure 18(b). Evaluated average strain range values are reported in Table 5, and these were used for the development of the proposed ULCF life prediction model.

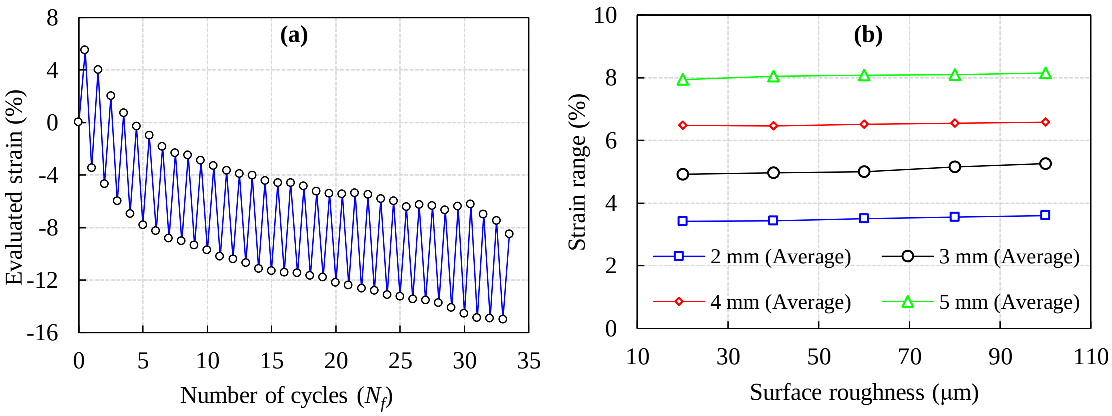

Figure 18. (a) Strain history of the "B20-CA5-0.005-Tri" specimen (b) Average strain range values for different surface roughness

4 Development of a new ULCF life prediction model

While developing the life prediction model, the main challenge was to choose the parameter that was closely correlated with the fatigue life. Since the damage to a material is related to its strain deformation, strain-based models are commonly used for predicting the LCF life (Tateishi et al., 2007) of metallic materials. Thus, the proposed model was also based on strain such that the effects of surface roughness and loading frequency on the fatigue life could be considered.

4.1 Basic Coffin–Manson relationship

Considering the wide application of the Coffin–Manson relationship to correlate LCF life and strain range (Tateishi et al., 2007) through a power law, the basic model was used in this study and formulated as

$$\Delta\varepsilon = c_1 N_f^{\alpha} \tag{4}$$

where $\Delta\varepsilon$ is the strain range and c_1 and α are the model parameters. Since plastic strain for the out of plane deformation was much larger than that in the elastic range, the total strain range was nearly equal to the plastic strain range, which was directly evaluated using the laser scanning technique. The model parameters were evaluated by fitting the experimental data of $\Delta\varepsilon$ versus N_f (fatigue life) at a given value of surface roughness and loading frequency (100 μm and 0.005 Hz, in this study). From Figure 19, we observed that the Coffin–Manson relationship could also correlate to the fatigue life of the considered SM400 steel.

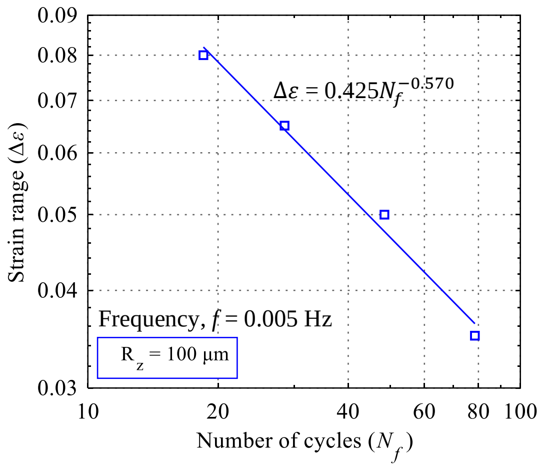

Figure 19. Correlating the strain range and fatigue life of SM400 using the Coffin–Manson relationship (log-log scale)

Table 8 contains the strain life relationships obtained from the present and previous studies (Sinsamutpadung et al., 2016; Usami et al., 2011) conducted on SM400 steel in the LCF regime. Results show that the tendency of power law relation fitted by current research agrees with the past research work.

The fatigue life of blasted specimens is lower than those of compact tension specimens tested by Sinsamutpadung et al., (2016), probably because of the influence of variable loading rate. However, the fatigue strength of buckling restrained braces provided in the reference (Usami et al., 2011) tested at the almost similar strain range is relatively lower than those of blasted specimens. This might be due to the influence of higher buckling mode which develops under the compression phase along with higher stress concentration around the welded joints of braces.

Table 8. Coffin Manson's relationships proposed by different studies

Name	Power law expressions
Present study	$\Delta\varepsilon = 0.425N_f^{-0.570}$
Sinsamutpadung et al., (2016)	$\Delta\varepsilon = 0.793N_f^{-0.451}$
Usami et al., (2011)	$\Delta\varepsilon = 0.210N_f^{-0.488}$

4.2 Characterizing the effect of surface roughness

As summarized in section 3.1, the fatigue life of steel under different surface roughness decreases with the increase in loading amplitudes, causing severe damage that leads to the fatigue failure of the steel specimens. Thus, the relationship between fatigue life and surface roughness was plotted on a linear scale by power fitting the data, as shown in Figure 20, which indicated a negative correlation. The power law function gave the best fit to the data set and was expressed as

$$N_f = c_2 R_z^{\beta} \tag{5}$$

Performing the logarithmic operation on equation (5) yielded

$$\log N_f = \log c_2 + \beta \log R_z \tag{6}$$

Thereafter, two important observations were made: ① irrespective of the strain range $\Delta\varepsilon$, the fatigue life N_f of steel decreased with an increase in surface roughness, confirming the reasonability of considering the effect of roughness on fracture in the Coffin–Manson model, and ② the exponents of the fitting lines were very close for different cases of strain ranges, as listed in Table 9. By assuming the exponent to be independent of strain range, a relation for characterizing the effect of surface roughness was obtained as

$$\log N_f - \log N_r = \beta \log(R_z/R_{zr}) \tag{7}$$

where R_{zr} is the reference surface roughness, corresponding to the experimental data used for fitting the basic model, and N_r is corresponding reference fatigue life.

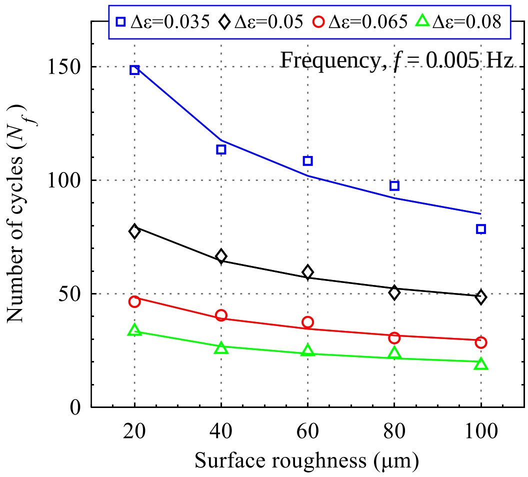

Figure 20. Characterizing the effect of surface roughness on the fatigue life (linear scale)

4.3 Characterizing the effect of loading frequency

From section 3.2, the fatigue life was interpreted to increase with an increase in loading frequency under different values of surface roughness. Moreover, the fatigue life at the surface roughness of 20 μm was higher than that at 100 μm. The relation between loading frequency and fatigue life, illustrated in Figure 21, indicated a positive correlation. The fatigue life on a logarithmic scale presented a linear correlation with the loading frequency. By power fitting the data presented in Figure 21, relevant equations of fitting lines were achieved and expressed as

$$N_f = c_3 f^{\gamma} \tag{8}$$

Performing the logarithmic operation on equation (8) yielded

$$\log N_f = \log c_3 + \gamma \log f \tag{9}$$

From Table 10, we can interpret that the exponents of the equations were close to each other. By considering the exponents to be slightly dependent on surface roughness, the change in fatigue life due to variable loading frequency was expressed as

$$\log N_f - \log N_r = \gamma \log(f/f_r) \tag{10}$$

where f_r is the reference loading frequency corresponding to the experimental data being used for fitting the basic model and N_r is the corresponding reference fatigue life.

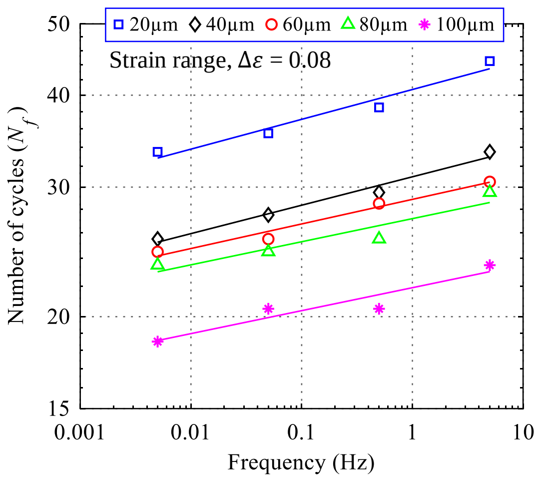

Figure 21. Characterizing the influence of loading frequency on the fatigue life (log-log scale)

4.4 Proposed life prediction model

In the preceding subsections, equations (4), (7), and (10) were obtained to characterize the impact of strain range, surface roughness, and loading frequency, respectively, on fatigue life. This subsection briefly discusses an introduction to the newly modified ULCF model. In this paper, reference values of surface roughness R_{zr} and loading frequency f_r were selected as 100 μm and 0.005 Hz, respectively. Firstly, the fatigue life (denoted as N_{ra}) at an arbitrary value of $\Delta\varepsilon$, a given frequency f_r = 0.005 Hz, and surface roughness R_{zr} = 100 µm was obtained on the basis of equation (4) as

$$N_{ra} = (\Delta\varepsilon/c_1)^{1/\alpha} \tag{11}$$

Performing the logarithmic operation on equation (11) yielded

$$\log N_{ra} = 1/\alpha(\log{(\Delta\varepsilon/c_1)}) \tag{12}$$

Thus, when the value of R_{zr} in equation (7) was fixed to 100 µm, N_r in equation (7) was actually equal to N_{ra}. Substituting N_{ra} as N_r in equation (7), the fatigue life (denoted by N_{rb}) at an arbitrary value of $\Delta\varepsilon$ and R_z for a given f_r was expressed as

$$\log N_{rb} - \log N_{ra} = \beta\log(R_z/R_{zr}) \tag{13}$$

$$\log N_{rb} = 1/\alpha(\log{(\Delta\varepsilon/c_1)}) + \beta\log(R_z/R_{zr}) \tag{14}$$

Similarly, after fixing f_r = 0.005 Hz in equation (14), N_r in equation (10) was replaced by N_{rb}. Thereafter, substituting N_{rb} as N_r in Eq. (10), a new ULCF life prediction model incorporating the effects of strain range, surface roughness, and loading frequency was expressed as

$$\log N_f - \log N_{rb} = \gamma\log(f/f_r) \tag{15}$$

$$\log N_f = 1/\alpha(\log{(\Delta\varepsilon/c_1)}) + \beta\log(\mathrm{R_z}/\mathrm{R_{zr}}) + \gamma\log(f/f_r) \tag{16}$$

where $\Delta\varepsilon$, R_z, and f are the strain range, surface roughness, and loading frequency, respectively; R_{zr} = 100 µm and f_r = 0.005 Hz are the reference surface roughness and loading frequency, respectively, determined by fitting the corresponding data; and c_1, α, β, and γ are the model parameters which are listed in Table 11. The model parameters β and γ were taken as the average slopes of the fitting lines as shown in Figures 20 and 21, respectively.

5 Model validation

Since the proposed fatigue life prediction model is purely empirical, its reliability must be validated through comprehensive experimental results. To verify its prediction accuracy, the proposed model was applied to all the test data listed in Tables 5, 6, and 7. Specifically, the validity of the proposed model was checked by applying the model to an unknown test dataset (not used for the development of the model) listed in Table 7. The specimens in this data set were tested under variable loading amplitude because real engineering structures experience cycles of variable amplitudes during their service life. The simplified fatigue life model as expressed by equation (4) was fitted to the experimental test results of steel specimen with variable surface roughness presented in Table 5, tested at constant loading amplitudes under a loading frequency of 0.005 Hz, for plotting the S-N curves shown in Figure 22. The parameters of the basic Coffin–Manson equation at five different roughness were extracted by performing linear regression analysis and the corresponding coefficients are summarized in Table 12.

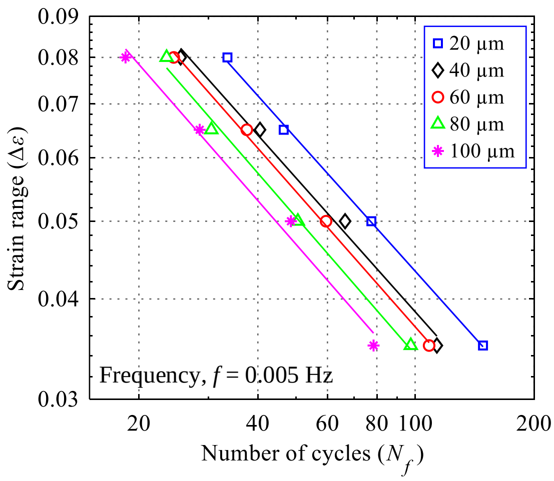

Figure 22. S-N Curves of SM400 using the Coffin–Manson relationship at different surface roughness (log-log scale)

Table 9. Coefficient c_2 and exponent β at four different strain ranges with f = 0.005 Hz

Coef.	Strain range, $\Delta\varepsilon$			
	0.035	0.05	0.065	0.08
c_2	430.70	195.75	120.90	86.10
β	-0.352	-0.301	-0.306	-0.316
R^2	0.949	0.970	0.926	0.924

Table 10. Coefficient c_3 and exponent γ at five different roughness with $\Delta\varepsilon$ = 0.08

Coef.	Surface roughness, R_z (μm)				
	20	40	60	80	100
c_3	40.71	30.98	28.87	27.18	21.89
γ	0.0405	0.0386	0.0334	0.0314	0.0312
R^2	0.9657	0.977	0.975	0.889	0.890

Table 11. Proposed model parameters

Model parameters	c_1	α	β	γ
	0.425	-0.570	-0.3035	0.03502

Table 12. Coefficient c_4 and exponent η at five different roughness

Coef.	Surface roughness, R_z (μm)				
	20	40	60	80	100
c_4	0.543	0.492	0.484	0.466	0.425
η	-0.549	-0.553	-0.559	-0.568	-0.570
R^2	0.998	0.992	0.997	0.991	0.992

Existing studies have indicated that Miner's rule results in an overestimation of fatigue life in the ULCF regime (Tateishi et al., 2007; Xue, 2008). Nevertheless, Miner's rule still gives accurate results when the largest applied strain range Δε is lesser than the damage strain threshold. True strain at the point of maximum tensile stress has been recommended as the damage strain threshold (Tateishi et al., 2007). In this study, the largest strain was 8% (Figure 18(b)), which was lesser than approximately 25% of the damage threshold value determined by conducting tension tests (Figure 1(b)). Accordingly, Miner's rule can be employed in this research study without any modification for the calculation of the equivalent strain range in the ULCF regime (Dehghani et al., 2017). The equivalent strain ranges under variable loading amplitude for each roughness case were expressed as (Tateishi et al., 2007)

$$\Delta\varepsilon_{eq} = \left(\frac{\sum(\Delta\varepsilon_i^{1/\eta}.n_i)}{N_f}\right)^{\eta} \tag{17}$$

$$N_f = \sum n_i \tag{18}$$

where $\Delta\varepsilon_{eq}$ is the equivalent strain range, η is the material constant, and n_i represents the number of loading cycles for the *i*th strain range. The calculated equivalent strain ranges are listed in Table 7. By using the calculated values, the fatigue life under variable loading amplitudes of all the blasted specimens in this group was predicted.

Figure 23 illustrates the comparison between experimental fatigue life N_f and predicted fatigue life $N_{f,p}$ of all the test specimens. The black dashed and solid red lines represent the $\pm$10% and $\pm$15% error bands, respectively. The efficacy of the proposed model for fatigue life estimation was estimated based on the percentage error (PE) calculated as PE = $1-|N_{f,p} - N_f|/N_{f,p}$ (Dehghani et al., 2017). Statistics of the percentage error provided information on the effectiveness of fatigue life estimation. Furthermore, average value (APE) and standard deviation (SD) of the PE were evaluated and highlighted in Figure 23 for each data set. In the case of specimens tested under constant loading amplitude with variable surface roughness as shown in Figure 23(a), out of a total of 20 data points, 19 points (95% data) were located within a $\pm$10% error band, while only 1 point fell in the $\pm$15% error band. A majority of the data points were below or close to the ideal regression line of 45°. Moreover, the APE and SD were 11.26% and 5.62%, respectively.

Considering the effects of variable frequency on the ULCF life as shown in Figure 23(b), all 20 points (100% data) for five different cases of roughness were located within an error band of $\pm$10%. For this

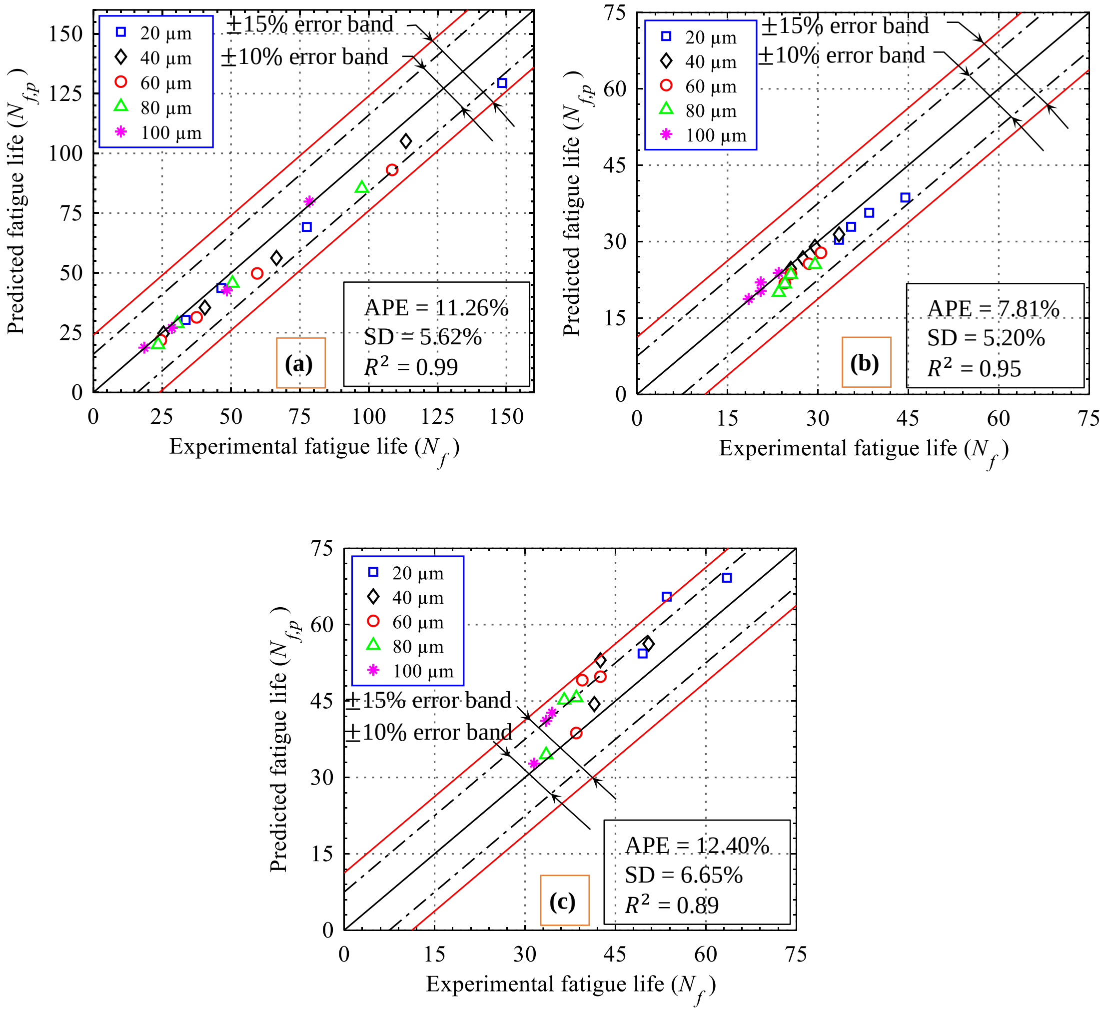

Figure 23. Comparison of the experimental and predicted fatigue life obtained using the proposed model (linear scale) under (a) constant loading amplitude, (b) loading frequency, and (c) variable loading amplitude

case, the calculated values of APE and SD were 7.81% and 5.20%, respectively, providing satisfactory results. The error between experimental and theoretical fatigue life for this data set ranged between 0.99 to 17.38%. Figure 23(c) presents the results of specimens under different variable loading amplitude patterns. Out of 15 points, 10 points were within the ±10% error band, 4 points fell inside an error band of ±15%, and only 1 point was outside the $\pm$15% error band. Under variable loading amplitude, 93% of data (14 data points) of the predicted fatigue life for the tested specimens were within an acceptable error band of $\pm$15%. Thus, the results showed that the proposed model was capable of predicting fatigue life in the case of variable loading patterns with reasonable accuracy. Considering the overall data set containing 55 specimens with variable surface roughness, 89% of data were within the $\pm$10% error band; 9% of data fitted inside the $\pm$15% error band; and only 2% of data fell outside the $\pm$15% error band, indicating the efficacy of the proposed model.

The proposed model comprising of equation (16) can be applied to the buckling prone structural members made up of SM400 steel such as lateral and sway bracings, vertical stiffeners, I-section girders, pipes, and piers with the similar condition of experimental specimens of this study. On the other hand, SM400 is one of the most commonly used structural steels in Japan. In order to clarify the generality of the model, further study targeting a wide range of steels and structural components is desirable.

6 Conclusions

In this study, a total of 59 displacement-controlled tests were conducted to study the effects of surface roughness, loading amplitudes, and loading frequencies on the fatigue life of SM400 structural steel in the ULCF regime. Based on the conventional fatigue theory and experimental data, a new mathematical model accounting for the combined effect of the aforementioned parameters is proposed. The model parameters are estimated by fitting the experimentally obtained data. Finally, variable and constant amplitude test results are used to validate the accuracy of the proposed model. The main conclusions of this study are summarized as follows:

1. The combined effects of surface roughness and loading amplitude have a significant impact on the ULCF life of structural steel. An increase in surface roughness and loading amplitude resulted in the acceleration of fatigue damage and earlier failure of steel specimens, which became more distinct at higher values. An increase in loading amplitude from 2 to 5 mm resulted in a 77% decrease in the

ULCF life for specimens of surface roughness 20 μm. On studying the effect of surface roughness, fatigue life was observed to decrease significantly by a factor of 1.89, from 148.5 to 78.5 cycles, with an increase in surface roughness from 20 to 100 μm at a loading amplitude of 2 mm.

2. From the experimental results, the ULCF life of the specimens was found to be evidently sensitive to variations in loading frequency. An increase in loading frequency from 0.005 to 5 Hz caused an increase of 33% in the fatigue life of specimens with 20 μm surface roughness. Additionally, on evaluating the impact of surface roughness, the fatigue life was observed to increase by a factor of 1.81, from 18.5 to 33.5 cycles, with a decrease in the surface roughness, from 100 to 20 μm at the loading frequency of 0.005 Hz. In addition, results demonstrated that the effects of loading amplitude on fatigue life were larger than those of loading frequency under a specified value of surface roughness.
3. Loading conditions have a substantial effect on the ULCF behavior of specimens. Blasted specimens subjected to higher loading frequency showed higher energy dissipation and late drop in peak load, indicating longer fatigue life. While those subjected to higher loading amplitude presented lower energy dissipation and earlier drop in peak load, highlighting a reduction in fatigue life.
4. A new ULCF life prediction model is proposed, which establishes a relation between the parameters of surface roughness, loading amplitude, loading frequency, and fatigue life. The predicted results corroborated well with the experimental data on the suitable selection of the model parameters. The analysis results showed that the predicted life for almost all the data was within an acceptable error band of $\pm$15%, while R^2 ranged from 0.89 – 0.99, representing the effectiveness of the proposed model.

To summarize, this study demonstrates the combined effects of surface roughness, loading frequency, and loading amplitude on the fatigue life of metal structures. The introduction of these parameters into the ULCF life estimation model extends its usefulness in various engineering applications whereby surface treatment of structures is indispensable. Thus, the proposed model is expected to assist structural engineers and researchers at the design and maintenance stages to accurately calculate the ULCF life and to prevent associated fatigue failures. This study can be further extended to future research to account for the effects of (1) other loading waveforms such as sinusoidal etc., (2) other specimen geometry such as thickness, width, length, etc., and (3) other types of steels on ULCF life.

Acknowledgements

The first author greatly acknowledges Dr. Khawaja Ali for his great support throughout this research work. The authors are grateful to Dr. Wang Jiaqi and Dr. Chang He for their assistance in carrying out the extensive experimentation.

Declaration of Conflicting Interests

The authors declare no personal or financial interests considering the current research, authorship, and publication of current work reported in this paper.

Funding

The author(s) received no financial support for the research, authorship, and/or publication of this article.

References

AASHTO (2012) *AASHTO LRFD Bridge Design Specifications*. 6th ed. Washington, DC: American Association of State Highway and Transportation Officials.

ASTM E1049 - 85 (2011) *Standard Practices for Cycle Counting in Fatigue Analysis*. American Society for Testing and Materials.

Nakajima K, Suzuki H, Kawabe Y, et al. (2011) Basic characteristics of high strength one-side bolted friction joints. *The 6th International Symposium on Steel Structures*: 641–648.

Dehghani M, Tremblay R and Leclerc M (2017) Fatigue failure of 350WT steel under large-strain seismic loading at room and subfreezing temperatures. *Construction and Building Materials* 145. Elsevier Ltd: 602–618.

FHWA (2015) *Steel Bridge Design Handbook on Corrosion Protection of Steel Bridges*. U.S. Department of Transportation Federal Highway Administration.

Ge H and Kang L (2012) A damage index-based evaluation method for predicting the ductile crack initiation in steel structures. *Journal of Earthquake Engineering* 16(5): 623–643.

Hasunuma S, Oki S, Motomatsu K, et al. (2019) Fatigue life prediction of carbon steel with machined surface layer under low-cycle fatigue. *International Journal of Fatigue* 123(February). Elsevier: 255–267.

ISO 8501 (2007) *Rust Grades and Preparation Grades of Uncoated Steels Substrates and of Steel Substrates after Overall Removal of Previous Coatings*. International Organization for Standardization.

ISO 8503-1 (2012) *Specifications and Definitions for ISO Surface Profile Comparators for the Assessment of Abrasive Blast-Cleaned Surfaces*. International Organization for Standardization.

JASS 6 (2007) *Japanese Architectural Standard Specification JASS 6: Structural Steelwork Specification for Building Construction*. Architectural Institue of Japan.

Jia LJ and Ge H (2018) *Ultra-Low-Cycle Fatigue Failure of Metal Structures under Strong Earthquakes*. Springer Singapore.

Jia LJ, Koyama T and Kuwamura H (2014) Experimental and numerical study of postbuckling ductile fracture of heat-treated SHS stub columns. *Journal of Structural Engineering* 140(7): 1–13.

JIS B 0601 (2013) *Geometrical Product Specifications (GPS)-Surface Texture: Profile Method - Terms, Definitions and Surface Texture Parameters ICS*. Japanese Standards Association.

JIS G 3106 (2004) *Rolled Steel for Welded Structure*. Japanese Standards Association.

Kainuma S (2021) Steel surface preparation by abrasive blast treatment in existing steel road bridges. *Journal of The Surface Finishing Society of Japan* 72(1): 12–16.

Kanchanomai C, Miyashita Y, Mutoh Y, et al. (2003) Influence of frequency on low cycle fatigue behavior of Pb-free solder 96.5Sn-3.5Ag. *Materials Science and Engineering A* 345(1–2): 90–98.

Kuroda M (2002) Extremely low cycle fatigue life prediction based on a new cumulative fatigue damage model. *International Journal of Fatigue* 24(6): 699–703.

L. F. Coffin J (1954) A Study of the effects of cyclic thermal stresses on a ductile metal. *Transactions of the American Society of Mechanical Engineers* 76(6): 931–949.

Lee JM, Kim YJ and Kim JW (2022) Very low cycle fatigue life evaluation models and validation using notched compact tension test data. *International Journal of Fatigue* 155(November 2021). Elsevier Ltd: 106635.

Li S, Xie X, Cheng C, et al. (2020) A modified Coffin-Manson model for ultra-low cycle fatigue fracture of structural steels considering the effect of stress triaxiality. *Engineering Fracture Mechanics* 237(December 2019). Elsevier: 107223.

Li S, Xie X, Tian Q, et al. (2021) A proposal on ultra-low cycle fatigue damage evaluation of structural steels. *Theoretical and Applied Fracture Mechanics* 114(March). Elsevier Ltd: 102973.

Luo YR, Huang CX, Tian RH, et al. (2013) Effects of strain rate on low cycle fatigue behaviors of high-strength structural steel. *Journal of Iron and Steel Research International* 20(7). Central Iron and Steel Research Institute: 50–56.

McKelvey SA and Fatemi A (2012) Surface finish effect on fatigue behavior of forged steel. *International Journal of Fatigue* 36(1). Elsevier Ltd: 130–145.

Miller DK (1998) Lessons learned from the Northridge earthquake. *Engineering Structures* 20(4–6): 249–260.

Miner MA (1945) Cummulative damage in fatigue. *Journal of Applied Mechanics* 12(3): A159–A164.

Nakashima M, Inoue K and Tada M (1998) Classification of damage to steel buildings observed in the 1995 Hyogoken-Nanbu earthquake. *Engineering Structures* 20(4–6): 271–281.

NILIM (2020) *Steel Highway Bridge Repainting Procedure (In Japanese)*. National Institute for Land and Infrastructure Management.

Nip KH, Gardner L, Davies CM, et al. (2010) Extremely low cycle fatigue tests on structural carbon steel and stainless steel. *Journal of Constructional Steel Research* 66(1). Elsevier Ltd: 96–110.

Park YS, Park SJ, Iwai S, et al. (2004) Failure and damage of steel thin-plate elements and angle members due to very-low-cycle loading. *Engineering Structures* 26(11): 1623–1632.

Pegues J, Roach M, Scott Williamson R, et al. (2018) Surface roughness effects on the fatigue strength of additively manufactured Ti-6Al-4V. *International Journal of Fatigue* 116(July). Elsevier: 543–552.

Poorna Chander K, Vashista M, Sabiruddin K, et al. (2009) Effects of grit blasting on surface properties of steel substrates. *Materials and Design* 30(8). Elsevier Ltd: 2895–2902.

RCSC (2020) *Specification for Structural Joints Using High-Strength Bolts*. Research Council on Structural Connections. Available at: www.boltcouncil.org.

Reddy GVP, Kannan R, Mariappan K, et al. (2015a) Effect of strain rate on low cycle fatigue of 316LN stainless steel with varying nitrogen content: Part-I cyclic deformation behavior. *International Journal of Fatigue* 81. Elsevier Ltd: 299–308.

Reddy GVP, Mariappan K, Kannan R, et al. (2015b) Effect of strain rate on low cycle fatigue of 316LN stainless steel with varying nitrogen content: Part-II fatigue life and fracture. *International Journal of Fatigue* 81. Elsevier Ltd: 309–317.

Salawdeh S and Goggins J (2013) Numerical simulation for steel brace members incorporating a fatigue model. *Engineering Structures* 46: 332–349.

Saleem A, Tamura H and Katsuchi H (2022) Change in surface topography of structural steel under cyclic plastic deformation. In: *Proceedings of the 9th International Conference on Fracture, Fatigue and Wear*. Springer Singapore, pp. 175–193.

Singh K, Sadeghi F, Correns M, et al. (2019) A microstructure based approach to model effects of surface roughness on tensile fatigue. *International Journal of Fatigue* 129(June). Elsevier: 105229.

Sinsamutpadung N and Sasaki E (2018) Effects of high strain rate on Low-Cycle Fatigue behavior of steel welded joints during earthquake loading. *International Journal of Steel Structures* 18: 793–801.

Sinsamutpadung N, Sasaki E and Tamura H (2016) Effects of high strain rate on low-cycle fatigue behavior of structural steel in large plastic strain region. *Journal of JSCE* 4(1): 118–133.

Song F, Xie X and Zhang T (2021a) Effect of corroded surface morphology on ultra-low cycle fatigue of steel plate. *materials* 43(5). MDPI: 132–141.

Song F, Zhang T and Xie X (2021b) Ultra-low cycle fatigue properties and fracture mechanism of corroded structural steel. *Corrosion Engineering Science and Technology* 56(7). Taylor & Francis: 626–638.

Tamura H, Sasaki E, Yamada H, et al. (2009) Involvements of stress triaxiality in the brittle fracture during earthquakes in steel bridge bents. *International Journal of Steel Structures* 9(3): 241–252.

Tamura H, Sasaki E, Hitoshi Y, et al. (2012) Study on the casue of brittle fracture during earthquakes in steel bridge bents focusing on dynamic load effect. *Journal of JSCE* 68(2): 226-241 (In Japanese).

Tamura H, Sasaki E and Tominaga S (2018) Modified-Weibull-stress-based evaluation of brittle fracture occurrence during earthquakes in steel members. *Engineering Fracture Mechanics* 202(August 2017). Elsevier: 375–393.

Tateishi K, Hanji T and Minami K (2007) A prediction model for extremely low cycle fatigue strength of structural steel. *International Journal of Fatigue* 29(5): 887–896.

Tian Q, Xie X and Li S (2021) A model for ultra low cycle fatigue damage prediction of structural steel. *Journal of Constructional Steel Research* 187(September). Elsevier Ltd: 106956.

Usami T, Wang C and Funayama J (2011) Low-cycle fatigue tests of a type of Buckling Restrained Braces. *Procedia Engineering* 14: 956–964.

Wang J, Zhang Y, Sun Q, et al. (2016) Giga-fatigue life prediction of FV520B-I with surface roughness. *Materials and Design* 89. Elsevier Ltd: 1028–1034.

Wang JL, Zhang YL, Zhao QC, et al. (2017) The fatigue failure analysis and fatigue life prediction model of FV520B-I as a function of surface roughness in HCF regime. *Journal of Materials Research* 32(3): 634–643.

Wang T, Wen JF, Liao PP, et al. (2021) A study of ultra-low cycle fatigue failure based on a fracture strain energy model. *International Journal of Fatigue* 146(October 2020). Elsevier Ltd: 1–14.

Wang Y, Meletis EI and Huang H (2013) Quantitative study of surface roughness evolution during low-cycle fatigue of 316L stainless steel using Scanning Whitelight Interferometric (SWLI) Microscopy. *International Journal of Fatigue* 48. Elsevier Ltd: 280–288.

Xiang P, Jia LJ, Shi M, et al. (2017) Ultra-low cycle fatigue life of aluminum alloy and its prediction using monotonic tension test results. *Engineering Fracture Mechanics* 186(November 2017). Elsevier Ltd: 449–465. DOI: 10.1016/j.engfracmech.2017.11.006.

Xie X, Cheng C and Li S (2020) A deformation history-based approach for ultra-low cycle fatigue damage evaluation of steel structures. *International Journal of Steel Structures* 20(4). Korean Society of Steel Construction: 1378–1392.

Xu F, Chan TM, Sheehan T, et al. (2020) Prediction of ductile fracture for circular hollow section bracing members under extremely low cycle fatigue. *Engineering Structures* 214(April). Elsevier: 110579.

Xue L (2008) A unified expression for low cycle fatigue and extremely low cycle fatigue and its implication for monotonic loading. *International Journal of Fatigue* 30(10–11): 1691–1698.

Zhao Z, Wang L, Zhang J, et al. (2021) Prediction of high-cycle fatigue strength in a Ti-17 alloy blade after foreign object damage. *Engineering Fracture Mechanics* 241(October). Elsevier Ltd: 107385.